November 1, 1994

Measurements of the electric and magnetic form factors of the proton from Q2=1.75 to 8.83 (GeV/c)2

L Andivahis
R S Hicks, *University of Massachusetts - Amherst*
R A Miskimen, *University of Massachusetts - Amherst*
Gerald Alvin Peterson, *University of Massachusetts - Amherst*
S Rokni, *University of Massachusetts - Amherst*

PHYSICAL REVIEW D VOLUME 50, NUMBER 9 1 NOVEMBER 1994

Measurements of the electric and magnetic form factors of the proton from $Q^2 = 1.75$ to $8.83\ (\text{GeV}/c)^2$

L. Andivahis,[1] P. E. Bosted,[1] A. Lung,[1,*] L. M. Stuart,[2,4,†] J. Alster,[12] R. G. Arnold,[1] C. C. Chang,[5]
F. S. Dietrich,[4] W. Dodge,[7,‡] R. Gearhart,[10] J. Gomez,[3] K. A. Griffioen,[8,§] R. S. Hicks,[6] C. E. Hyde-Wright,[13,‖]
C. Keppel,[1] S. E. Kuhn,[11,‖] J. Lichtenstadt,[12] R. A. Miskimen,[6] G. A. Peterson,[6] G. G. Petratos,[9,¶] S. E. Rock,[1]
S. Rokni,[6,†] W. K. Sakumoto,[9] M. Spengos,[1] K. Swartz,[13] Z. Szalata,[1] and L. H. Tao[1]
[1] *The American University, Washington, D.C. 20016*
[2] *University of California, Davis, California 95616*
[3] *Continuous Electron Beam Accelerator Facility, Newport News, Virginia 23606*
[4] *Lawrence Livermore National Laboratory, Livermore, California 94550*
[5] *University of Maryland, College Park, Maryland 20742*
[6] *University of Massachusetts, Amherst, Massachusetts 01003*
[7] *National Institute of Standards and Technology, Gaithersburg, Maryland 20899*
[8] *University of Pennsylvania, Philadelphia, Pennsylvania 19104*
[9] *University of Rochester, Rochester, New York 14627*
[10] *Stanford Linear Accelerator Center, Stanford, California 94309*
[11] *Stanford University, Stanford, California 94305*
[12] *University of Tel-Aviv, Ramat Aviv, Tel-Aviv 69978, Israel*
[13] *University of Washington, Seattle, Washington 98195*
(Received 24 March 1994)

The proton elastic form factors $G_{E_p}(Q^2)$ and $G_{M_p}(Q^2)$ have been extracted for $Q^2 = 1.75$ to $8.83\ (\text{GeV}/c)^2$ via a Rosenbluth separation to *ep* elastic cross section measurements in the angular range $13^\circ \leq \theta \leq 90^\circ$. The Q^2 range covered more than doubles that of the existing data. For $Q^2 < 4\ (\text{GeV}/c)^2$, where the data overlap with previous measurements, the total uncertainties have been reduced to $< 14\%$ in G_{E_p} and $< 1.5\%$ in G_{M_p}. Results for $G_{E_p}(Q^2)$ are consistent with the dipole fit, $G_D(Q^2) = (1 + Q^2/0.71)^{-2}$, while those for $G_{M_p}(Q^2)/\mu_p G_D(Q^2)$ decrease smoothly from 1.05 to 0.92. Deviations from form factor scaling are observed up to 20%. The ratio Q^2F_2/F_1 is observed to approach a constant value for $Q^2 > 3\ (\text{GeV}/c)^2$. Comparisons are made to vector meson dominance, dimensional scaling, QCD sum rule, diquark, and constituent quark models, none of which fully characterize all the new data.

PACS number(s): 13.40.Gp, 12.38.Qk, 13.60.Fz, 14.20.Dh

I. INTRODUCTION

Understanding the strong force which binds neutrons and protons together to form nuclei has been a focal point in nuclear physics for nearly half a century. It is currently believed that the key to understanding the strong interaction lies within the theory of quantum chromodynamics (QCD) which governs the interaction among quarks and gluons. Perturbative techniques, similar to those of quantum electrodynamics (QED), have been applied to QCD in the region of large four-momentum transfer squared Q^2, and have successfully predicted the large Q^2 behavior of exclusive reactions [1]. However, because of the Q^2 dependence of the strong coupling constant,

$$\alpha_s(Q^2) \propto \frac{1}{\ln(Q^2/\Lambda^2_{\text{QCD}})}, \tag{1}$$

perturbation theory cannot be applied for $Q^2 \sim O(\Lambda^2_{\text{QCD}})$, where Λ_{QCD} is a scale factor resulting from renormalization in QCD. Experimental results [2] show $\Lambda_{\text{QCD}} \simeq 0.2$ GeV.

A great deal of hadronic physics takes place in the low to moderate Q^2 range which cannot be treated by techniques of perturbative QCD (PQCD). One such example, which is the subject of this paper, is the Q^2 dependence of the electromagnetic form factors of the nucleon. The form factors parametrize the internal structure of the nucleon as viewed by the virtual photon probe in elastic electron-nucleon scattering, for which the internal constituents of the nucleon remain in their ground state upon absorption of a virtual photon. The electron-

---

[*] Present address: California Institute of Technology, Pasadena, CA 91125.

[†] Present address: Stanford Linear Accelerator Center, Stanford, CA 94309.

[‡] Present address: George Washington University, Washington, D.C. 20052.

[§] Present address: The College of William and Mary, Williamsburg, VA 23187.

[‖] Present address: Old Dominion University, Norfolk, VA 23529.

[¶] Present address: Kent State University, Kent, OH 44242.

0556-2821/94/50(9)/5491(27)/$06.00

photon scattering vertex is well understood within the theory of QED, and the unknown details of the photon-nucleon vertex can be expressed in terms of two electromagnetic form factors $G_E(Q^2)$ and $G_M(Q^2)$, which parametrize the electric and magnetic charge distributions, respectively, within the nucleon. The form factors are functions of Q^2 only, and can be extracted from measurements of elastic electron-nucleon scattering.

Previous measurements of both nucleon form factors separately have been confined to relatively low Q^2. In the case of the proton, they have been independently measured [3–7] up to $Q^2 \simeq 4$ (GeV/c)^2, while for the more difficult case of the neutron, they have been separated [3,8,9] up to $Q^2 \simeq 2.6$ (GeV/c)^2, but with much larger errors. When form factor scaling ($G_E = G_M/\mu_p$) is assumed, the magnetic form factors of the proton and neutron have been extracted out to $Q^2 \simeq 31$ (GeV/c)^2 and 10 (GeV/c)^2, respectively, using forward-angle elastic cross section data [10,11]. These results indicate that the form factors fall with Q^2 according to a dipole form:

$$G_D(Q^2) = \left(1 + \frac{Q^2}{0.71}\right)^{-2}, \tag{2}$$

where the parameter 0.71 (GeV/c)^2 comes from a fit to existing data. However, a closer look at the behavior of the proton form factors in the region of $Q^2 = 2 - 3$ (GeV/c)^2 where the error bars are small, suggests deviations from a dipole dependence by as much as 10–20 %.

The low Q^2 data have been described within the framework of vector meson dominance (VMD) models which depict the photon-nucleon interaction in terms of an intermediary coupling of the photon to vector meson resonant states or $q\bar{q}$ pairs. Although the VMD models are successful in describing the low Q^2 data, they break down at high Q^2 and are unable to explain the scaling found in deep inelastic scattering without the unattractive inclusion of an infinite number of vector mesons. On the other hand, at high Q^2 the photon is considered to interact directly with the valence quarks, and PQCD is believed to give the correct asymptotic Q^2 dependence. For the moderate Q^2 range [the limits of which are not clearly defined, but typically $1 - 20$ (GeV/c)^2] neither PQCD nor the meson description are able to fully characterize all of the data. The intermediate Q^2 region is very important because it is at these momentum transfers that the virtual photon becomes sensitive to the internal quark structure of the nucleon, and the transition from photon-meson coupling to photon-quark coupling takes place.

To provide valuable constraints on competing models we have made precision measurements of the proton and neutron form factors in the moderate Q^2 region. This paper presents details of the proton analysis and results previously described only briefly [12]. A detailed paper on the neutron form factors [13] is planned for the future.

A. Elastic electron-proton scattering and electromagnetic form factors

The Feynman diagram for elastic electron-proton scattering in the single photon approximation is shown in Fig. 1. An electron with initial and final four-momenta given by k_μ and k'_μ, respectively, scatters elastically from a proton at rest in the laboratory frame, with corresponding initial and final four-momenta given by p_μ and p'_μ, respectively. The four-momentum transfer q carried by the virtual photon is constrained by momentum conservation to be $q = (k_\mu - k'_\mu)$. The square of the four-momentum transfer is a Lorentz invariant and is given in terms of the incident energy E, the final energy E', and the scattering angle θ as follows:

$$Q^2 \equiv -q^2 = 4EE' \sin^2(\theta/2), \tag{3}$$

where the mass of the electron has been neglected since $E \gg m_e$. Elastic scattering requires that the proton remain bound after the exchange of a virtual photon. Thus, $p'_\mu p'^\mu = M_p^2$, where M_p is the rest mass of the proton, and this gives rise to the condition required for elastic scattering:

$$x \equiv \frac{Q^2}{2M_p\nu} = 1, \tag{4}$$

where $\nu = E - E'$ is the energy transferred to the proton.

The differential cross section for $ep \to ep$ can be expressed as

$$\frac{d\sigma}{d\Omega} = \sigma_{\rm ns}\left\{F_1^2(Q^2) + \frac{\kappa_p^2 Q^2}{4M_p^2}F_2^2(Q^2) + \frac{Q^2}{2M_p^2}\left[F_1(Q^2) + \kappa_p F_2(Q^2)\right]^2 \tan^2(\theta/2)\right\}, \tag{5}$$

where

$$\sigma_{\rm ns} = \frac{\alpha^2 \cos^2(\theta/2)}{4E^2 \sin^4(\theta/2)}\frac{E'}{E} \tag{6}$$

is the nonstructure cross section, $\kappa_p = 1.7928...$ nm is the proton anomalous magnetic moment, and $F_1(Q^2)$ and $F_2(Q^2)$ are known as the Dirac and Pauli form factors, respectively. These form factors depend on Q^2 only and parametrize the internal structure of the proton. They are normalized so that in the limit $Q^2 \to 0$, when the virtual photon becomes insensitive to the proton structure, the proton coupling reduces to that of a pointlike charge. Thus,

$$F_1(0) = 1 \text{ and } F_2(0) = 1. \tag{7}$$

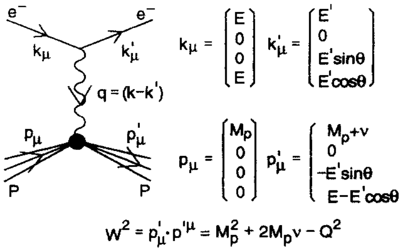

FIG. 1. Feynman diagram for elastic electron-proton scattering in the single photon approximation. Elastic scattering requires $W^2 = M_p^2$, giving rise to the condition $Q^2 = 2M_p\nu$, where $\nu = E - E'$ and $Q^2 = -q^2 = 4EE' \sin^2(\theta/2)$.

In practice the cross section is often rewritten in terms of the Sachs form factors $G_{E_p}(Q^2)$ and $G_{M_p}(Q^2)$, which can be expressed as linear combinations of the Dirac and Pauli form factors as

$$G_{E_p}(Q^2) \equiv F_1(Q^2) - \frac{\kappa_p Q^2}{4M_p^2} F_2(Q^2), \qquad (8)$$

$$G_{M_p}(Q^2) \equiv F_1(Q^2) + \kappa_p F_2(Q^2), \qquad (9)$$

with normalizations at $Q^2 = 0$ given by

$$G_{E_p}(0) = 1 \qquad \text{and} \qquad G_{M_p}(0) = \mu_p, \qquad (10)$$

where $\mu_p = 1 + \kappa_p$ is the proton magnetic moment. In terms of the Sachs form factors, the expression for the differential cross section becomes

$$\frac{d\sigma}{d\Omega} = \sigma_{\rm ns} \left(\frac{G_{E_p}^2(Q^2) + \tau G_{M_p}^2(Q^2)}{1+\tau} + 2\tau G_{M_p}^2(Q^2) \tan^2(\theta/2) \right), \qquad (11)$$

where $\tau = Q^2/4M_p^2$. This form of the cross section is known as the Rosenbluth formula [14].

B. Form factor measurement

The Rosenbluth formula can be written in a form which allows the form factors to be separated:

$$\sigma_R \equiv \frac{d\sigma}{d\Omega} \frac{(1+\tau)\epsilon}{\sigma_{\rm ns}\tau} = \frac{\epsilon}{\tau} G_{E_p}^2(Q^2) + G_{M_p}^2(Q^2), \qquad (12)$$

where the reduced cross section σ_R is a product of the measured differential cross section and known kinematic factors. The quantity ϵ is a measure of the longitudinal polarization of the virtual photon. For a fixed value of Q^2 it depends only on the scattering angle θ:

$$\epsilon = \left\{1 + 2(1+\tau)\tan^2(\theta/2)\right\}^{-1}, \qquad (13)$$

$$0 \le \epsilon \le 1. \qquad (14)$$

Since the reduced cross section is linear in ϵ for fixed Q^2, the form factors can be extracted from a linear fit to reduced cross-section measurements made at constant Q^2 but varying ϵ values. This method, known as a Rosenbluth separation, yields $G_{E_p}^2/\tau$ as the slope, and $G_{M_p}^2$ as the intercept. Since $\tau \propto Q^2$, as Q^2 increases, the reduced cross section becomes predominantly a measure of G_{M_p}, and precision measurements of G_{E_p} become more difficult. Thus, the Rosenbluth separation technique of extracting form factors is limited at large Q^2.

C. This experiment

Experiment NE11 was performed at the Stanford Linear Accelerator Center (SLAC) in January and February of 1989. Both liquid hydrogen and liquid deuterium targets were used to measure *ep* elastic and *ed* quasielastic cross sections, making it possible to separate both the proton [12,15] and neutron [13,16,17] form factors within a single experiment. The Rosenbluth method was used to separate the proton and neutron form factors out to Q^2 of 8.83 and 4.00 $(\text{GeV}/c)^2$, respectively. In addition, measurements of the $\Delta(1232)$ form factor [17,18], as well as aluminum cross-section data [16,19] were also obtained.

The primary goal of the experiment was to minimize both statistical and systematic uncertainties while simultaneously extending the measurements to the maximum attainable Q^2 limit. Improvements in detector hardware, a wire float calibration of the 8 GeV spectrometer optics, up-graded klystrons in the accelerator, and the use of two spectrometers to measure events simultaneously, combined to allow considerably reduced errors compared to previous measurements.

II. EXPERIMENTAL APPARATUS

The SLAC Nuclear Physics Injector supplied a pulsed electron beam with energies ranging from 1.5 to 5.5 GeV and a pulse width of 2 μs in the normal mode, and an energy of 9.8 GeV with a pulse width 0.15 μs in the SLAC Energy Doubler (SLED) mode. The beam repetition rate was 120 pulses per second, with peak currents of 60 mA, and average currents ranging from 0.5 to 10 μA.

The electron beam entered into End Station A (ESA), which housed the target assembly and spectrometers, after first traversing through the *A*-line beam transport system. Figure 2 shows the configuration of the target and spectrometers during NE11. The beam entered at the left and passed through two toroidal charge monitors before striking the target located on the pivot. Two magnetic spectrometers, having maximum momenta of 1.6 GeV and 8 GeV, respectively, were used to detect scattered electrons simultaneously, while the majority of the beam passed on to Beam Dump East. The SLAC 1.6 GeV spectrometer was configured with two additional quadrupole magnets, in addition to the single 90° vertical bend dipole magnet, to increase the solid angle by

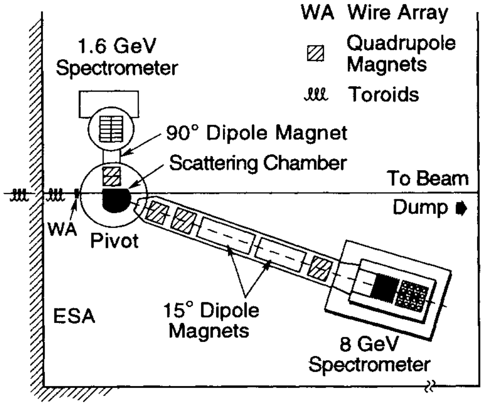

FIG. 2. A bird's eye view of the spectrometers and target area for NE11. The beam entered from the left and passed through two toroidal charge monitors before striking the target located on the pivot.

a factor of 3. Since the quadrupoles were placed on the pivot platform, the spectrometer remained fixed at 90° for the duration of the experiment. The 8 GeV spectrometer consists of two 15° vertical bend dipole magnets and three quadrupole magnets. It was rotated between 13.2° and 90°. Both spectrometers were equipped with similar detector packages consisting of a threshold Čerenkov detector, wire chambers, scintillators, and a lead glass shower counter array.

The target assembly contained liquid hydrogen and liquid deuterium cells as well as aluminum dummy targets needed to determine cell–end-cap subtractions. The targets were aligned on a vertical shaft which could be positioned remotely to select the desired target and place it in the path of the beam. The entire target assembly was contained in high vacuum within the scattering chamber and was placed at the spectrometer pivot. Thin aluminum windows separated the scattering chamber vacuum from the beam pipe vacuum, the 1.6 GeV spectrometer pipe vacuum, and the small air gap between the scattering chamber and the 8 GeV spectrometer. Since the 8 GeV spectrometer was not physically connected to the scattering chamber, an additional thin window of Mylar was used to separate the 8 GeV spectrometer pipe vacuum from the air gap.

Signals from the detectors were transmitted by heliac cables ($\beta \simeq 0.99$) to the event trigger electronics, or by coaxial signal cables ($\beta \simeq 0.66$) otherwise. The signals were processed by CAMAC and NIM electronic modules and sent to a PDP-11 computer. Event information was transferred from the PDP-11 to a Vax 11/780 which served as the primary source of computing power. A MicroVax II computer controlled the beam steering and charge measurements.

A. The electron beam

1. *Beam transport and energy measurement*

The beam energy was defined by eight identical dipole magnets through which the beam was deflected in the A-line transport system. A rotating flip coil located in a ninth magnet, identical to and in series with the others, but not in the path of the beam, continuously measured the beam energy. The flip coil reading was recorded every ten seconds and had an accuracy of ±0.1%. The spread in beam energy, $\Delta E/E$, was regulated by movable slits located downstream of the energy-defining dipole magnets. The slits were adjusted depending on the quality of the beam, its current and its energy, and were typically set between 0.1% and 0.5% (full width at half maximum) throughout the experiment.

The beam position and angle at the target were monitored continually and adjusted when necessary to maintain the beam position within ±1 mm of the target center, and the entrance angle within ±0.05 mr of the beam center line. This was achieved using the Beam Control System operating on the MicroVax computer. In order to determine the position and angle of the beam on the targets, this system relied upon a resonant microwave cavity located 52 m upstream of the target, and a set of secondary emission wire arrays just 2 m in front of the target. The wire array set consisted of two planes of 0.127 mm diameter aluminum wires spaced 0.635 mm apart. In one plane the wires were horizontal, in the other they were vertical. The resonant cavity provided a measurement of the lateral and vertical beam position relative to the cavity central axis.

2. *Toroidal charge monitors*

The incident charge per pulse was measured using two identical but independent toroidal charge monitors, Toroid_1 and Toroid_2, located inside the beam pipe approximately 10 m upstream of the target. The toroids were independently calibrated by sending pulses of known charge through the toroid via a calibration circuit. The charge was produced by allowing a capacitor to discharge through a single turn of wire which passed through the toroids. Both the capacitance and the voltage were known to ±0.1%. An attenuator circuit near the toroids was set remotely to values of 1, 10, or 100 such that a range of charges could be simulated. The calibration pulse was processed just as a beam pulse, and the relationship between the known calibration charge and the induced resonant signal was determined.

Corrections for time-dependent drifts in amplifier gains and calibrators were applied to each toroid reading. The typical size of the correction was a few tenths of a percent. The corrected toroid readings agreed on average to 0.16%, as indicated in Fig. 3, and were consistent with run-to-run fluctuations of ±0.2%. The charge per run, Q_i, was determined by the average of the integrated readings for the two toroids. A statistical uncertainty of ±0.2% was assigned based on the observed run-to-run fluctuations, and an overall normalization uncertainty of ±0.5% was assigned based on comparison with Faraday cup measurements.

B. Targets

The target assembly, illustrated in Fig. 4, contained four liquid cells (both long and short hydrogen and deuterium targets), and two aluminum targets. The long hydrogen and deuterium targets, nominally 15 cm, were

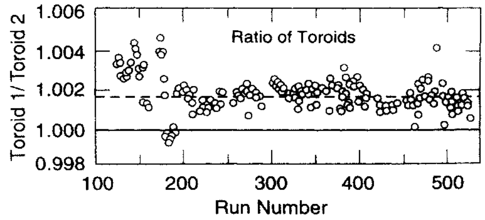

FIG. 3. The ratio of corrected toroid readings. The dashed line corresponds to the average value for the ratio over all runs, demonstrating that the two toroids agreed to 0.16%. Run-to-run fluctuations are consistent with ±0.2%.

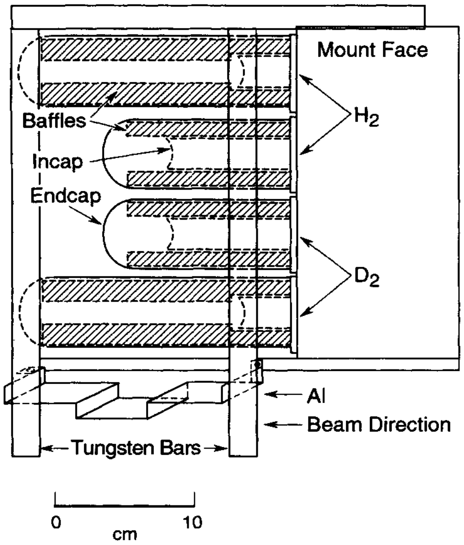

FIG. 4. Schematic of liquid and aluminum targets. The liquid target cells were constructed from beverage cans machined of a single piece of aluminum.

used to take the proton elastic and deuterium quasielastic data, while the 15 cm aluminum target was used to measure contributions to the 8 GeV spectrometer cross sections due to scattering from the aluminum end caps of the liquid targets. Since the 1.6 GeV spectrometer remained fixed at 90°, we were able to shield the spectrometer from electrons scattering from the aluminum end caps by placing two vertical tungsten bars on the target mount. The short 4 cm targets were used in special data runs as a check on the aluminum background subtraction.

The liquid target cells were constructed from beverage cans machined of a single piece of aluminum, thereby eliminating a soldering joint to adhere the end cap to the cell body. The beverage can was a significant improvement over previous target cells since its walls and end caps were made of a measurable uniform thickness, opposed to the varying thickness previously encountered in the solder joint. The aluminum targets were not replicas of the liquid targets, but instead were made from a single piece of aluminum, 0.63 mm thick, folded such that, depending on its vertical position, two ends either 15 cm apart or 4 cm apart would be in the path of the beam. The ends were angled at 45° to the beam and provided a total of 0.02 radiation lengths, which was nearly equivalent to the number of radiation lengths in the 15 cm hydrogen target. Table I gives a complete list of the material composition and thickness of the target cells and scattering chamber.

The liquid targets were maintained at roughly 21 K through constant contact with a reservoir of liquid hydrogen. The liquid hydrogen and deuterium within the targets were 99.9% and 99.0% pure, respectively, and were circulated at a rate of 2 m/s via flow guides. The target cells were kept in a high insulating vacuum $\simeq 10^{-7}$ torr, and the liquid was at a pressure of 2 atm. Vapor

TABLE I. Target cell and scattering chamber dimensions. The liquid target lengths are the calculated, contracted lengths at 21 K which are 0.996 times the measured lengths at room temperature. The aluminum target length is the total thickness viewed by the beam. The letters (*b*) and (*a*) denote whether the material is encountered before or after the scattering interaction, respectively.

Item		Material	Density (g/cm^3)	Length (cm)	X_o (g/cm^2)	Radiation lengths
Items upstream of target cell						
Set of wire arrays	(*b*)	Pure Al	2.70	0.00400	24.01	0.0004
Beam pipe window	(*b*)	Pure Al	2.70	0.00254	24.01	0.0003
Target cells						
In cap	(*b*)	Al 5052	2.68	0.00762	23.63	0.0009
Cell wall	(*a*)	Al 3004	2.72	0.01270	23.64	0.0015
End cap	(*a*)	Al 3004	2.72	0.01143	23.64	0.0013
Insulation	(*a*)	Mylar	1.39	0.00635	39.95	0.0002
Hydrogen (15 cm)	(*b*/*a*)	H	0.0707	14.9880	61.28	0.0173
Hydrogen (4 cm)	(*b*/*a*)	H	0.0707	3.9959	61.28	0.0046
Deuterium (15 cm)	(*b*/*a*)	D	0.1698	14.9248	122.60	0.0207
Deuterium (4 cm)	(*b*/*a*)	D	0.1698	4.0060	122.60	0.0055
Dummy cell (15 cm)	(*b*/*a*)	Al 6061	2.70	0.17900	23.39	0.0207
Dummy cell (4 cm)	(*b*/*a*)	Al 6061	2.70	0.17900	23.39	0.0207
Items downstream of target cell						
1.6 GeV chamber window	(*a*)	Al 5052	2.68	0.00762	23.63	0.0009
8 GeV chamber window	(*a*)	Al 5052	2.68	0.03048	23.63	0.0035
8 GeV beam pipe window	(*a*)	Mylar	1.39	0.03048	39.95	0.0011
8 GeV air gap	(*a*)	Air	0.00121	16.0	36.97	0.0005

pressure bulbs and platinum resistors, placed at the inlet and outlet valves of each target, were used to monitor the target density, ρ, determined by the average of the readings from the bulbs and the resistors. Corrections to the nominal density of 0.0707 g/cm^3 were applied per run, in accord with the observed dependence on beam current as illustrated in Fig. 5. For fixed beam intensity, run-to-run fluctuations in target density were consistent with a statistical uncertainty of ±0.2%. An overall normalization uncertainty of ±0.9% was assigned based on calibration data for the bulbs and resistors, and cryogenic data [20,21] needed to convert from raw measurements to temperature. Special data runs taken to study the possibility of local density fluctuations and target boiling along the path of the beam, indicated no changes on the level of 1%.

C. The 8 GeV spectrometer

1. Optics

The 8 GeV spectrometer [22] consists of three focusing quadrupoles and two 15° vertical bend dipoles configured as illustrated in Fig. 6. The optics [23] are line-to-point in the horizontal plane and point-to-point in the vertical plane as shown in Fig. 7. The nominal ranges spanned by the differential horizontal and vertical scattering angles, $\Delta\Theta$ and $\Delta\Phi$, were ±8 mr and ±28 mr, respectively, and the fractional momentum, $\delta = \Delta P/P$ ranged from -5% to 5% of the central value, yielding a relatively small solid angle of 0.7 msr. The reverse matrix elements were measured in a floating wire calibration [24] and are given in Ref. [15]. Typical resolutions were ±0.15% in momentum and ±0.5 mr in production angle.

The spectrometer was operated for a wide range of central momenta, $0.6 - 7.7$ GeV/c, measured to an accuracy of ±0.01% using nuclear magnetic resonance (NMR) probes installed in the dipole magnets. Similar high precision Hall probes were placed in the quadrupole fringe fields to indicate changes in field. All magnets were set according to a predetermined hysteresis curve or "degaussing cycle" to ensure that correct and reproducible field values were attained for each set point. Comparison between NMR measurements for each dipole indicated that the two fields agreed to within ±0.05%.

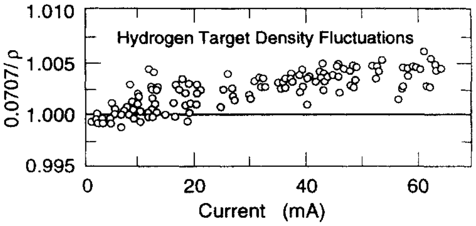

FIG. 5. Hydrogen target density versus peak beam current for all runs. This plot illustrates the expected slight decrease in density, ρ, with increased beam current. For fixed beam intensity, run-to-run fluctuations are consistent with ±0.2%.

2. Detectors

As indicated in Fig. 8, the first detector encountered by the particles was a gas-filled Čerenkov counter. The counter was 3.3 m long with 0.41 mm thick aluminum entrance and exit windows. A curved mirror with an area of 53 by 90 cm was located 3.15 m from the entrance window. Its aluminum surface was coated onto a 6.4 mm thick Lucite backing, and then covered with a layer of MgF$_2$ to help prevent oxidation. The mirror focused the Čerenkov light onto an RCA 8854 phototube, the face of which was coated with a wavelength shifter to improve light collection in the ultraviolet region. The Čerenkov counter was filled with nitrogen gas at 450 mm of Hg. The index of refraction at 0° C of 1.000165 yielded a pion threshold of 7.7 GeV and an electron threshold of 0.028 GeV. An average of 52 photons were emitted over the length of the counter, and the probability of a pion creating a knock-on electron above the Čerenkov threshold while traversing the aluminum entrance window and the nitrogen gas ranged from 0.04 to 0.09% for pion energies of 1.5 to 7.5 GeV.

Following the Čerenkov detector were ten planes of

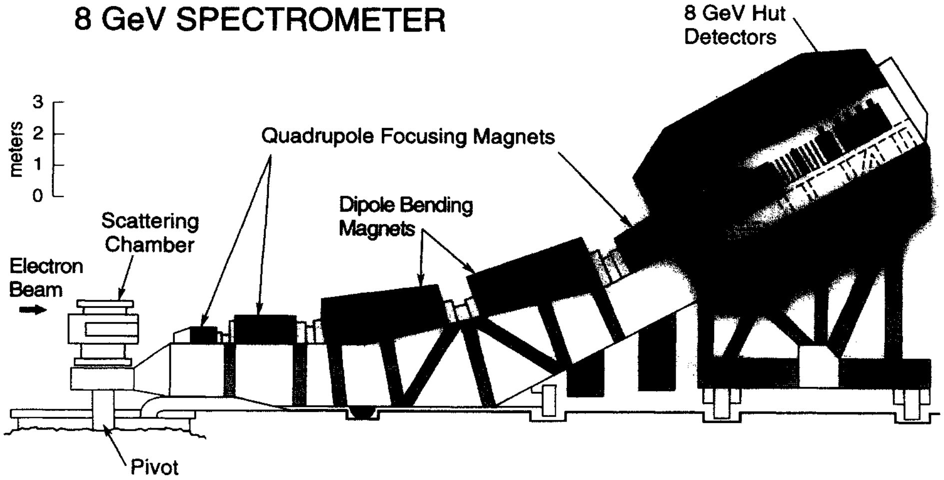

FIG. 6. The 8 GeV spectrometer. Three quadrupoles Q81, Q82, and Q83, provided focusing while two 15° vertical bend dipoles B81 and B82 provided the momentum dispersion. The spectrometer was rotated between 13.2° – 90°, and operated at central momenta between 0.6 – 7.7 GeV/c.

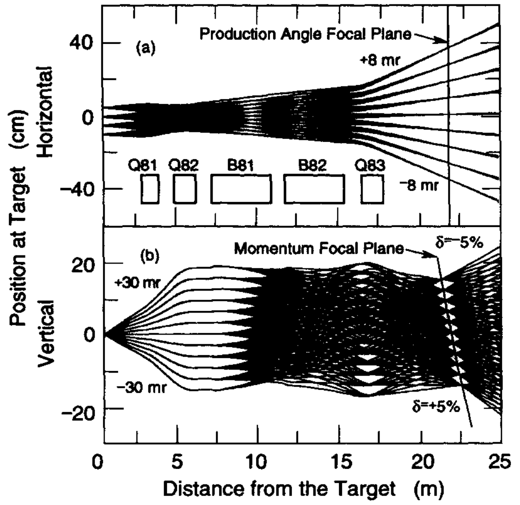

FIG. 7. The horizontal (a) and vertical (b) optics for the 8 GeV spectrometer. The boxes indicate the location of the magnets. The momentum focal plane is tilted at a steep angle of 13.9° relative to the central ray due to chromatic aberrations.

proportional wire chambers [25] used to reconstruct particle tracks. Each chamber contained a plane of gold-plated tungsten anode wires (20 μm diameter) sandwiched between two cathode planes of aluminum-coated Mylar. The separation between the anode and cathode planes was 4 mm. The cathode planes were kept at a voltage of -3.6 kV. A gas mixture consisting of 65.75% argon, 30.0% isobutane, 0.25% Freon 13B1, and 4% methyl-alcohol, circulated through the chambers at a rate of 5 cc/min. Each plane had an active area of 35 cm in height and 93 cm in width.

The chamber array was configured with alternating P and Θ chamber types. The P chambers had 176 horizontal wires spaced 2 mm apart which were used to measure the vertical position of the particle and thus its momentum. The position of a vertical Teflon support wire, attached near the center of each P chamber, was staggered in each chamber since these wires created a 2 cm wide dead region. The Θ chambers consisted of 480 wires spaced 2 mm apart. However, since pairs of adjacent wires were connected together electrically, there were effectively only 240 wires spaced 4 mm apart. The wires were strung at angles of either $+30°$ or $-30°$ to the vertical, and provided a measure of the particle horizontal position once the vertical position was known.

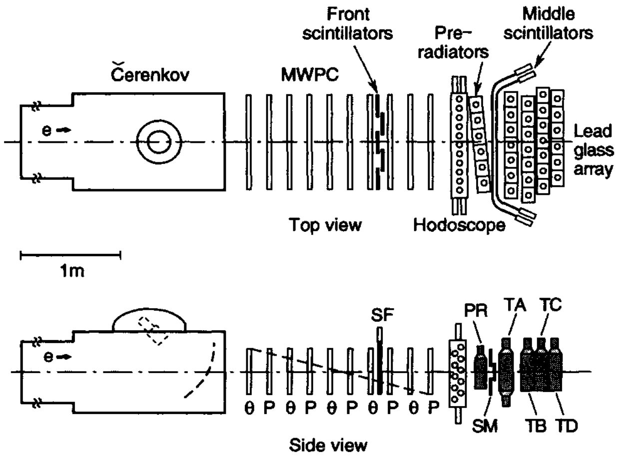

FIG. 8. The 8 GeV detectors. The detector package contained a nitrogen-filled Čerenkov detector followed by ten planes of multiwire proportional chambers and a lead glass shower counter. Two planes of scintillators were interspersed and a hodoscope was installed prior to the lead glass array. The momentum focal plane cuts diagonally through the wire chambers as indicated by the dashed line.

Signals from the hit wires were sent to circuit boards mounted directly on the chambers. Each board contained eight amplifiers and dual one-shot delays for use with eight wires. The two delays were timed for 500 ns each, for a total of 1000 ns, and the first determined the dead-time for the wire. The raw wire-chamber signals were processed into 16 bit words, each word corresponding to a group of adjacent wires that fired. A maximum of 64 words, or equivalently groups, was stored per trigger. The first three bits of each word gave the number of wires which fired in that group up to a maximum of seven. The remaining thirteen bits gave the wire number of the last wire that fired.

The lead glass shower counter was used to discriminate between electrons and pions by the energy deposited in the counter per incident momentum. The 8 GeV shower counter contained five rows of lead glass blocks; however since the shower was contained in the first four rows, the last row was not used. Each row contained six or seven blocks equipped with Amperex XP2041 phototubes. The first row, called the preradiator (PR), contained six F-2 type Pb glass blocks, and was oriented at an angle of 84.8° with respect to the central ray. This slight rotation from 90° minimized the number of particles passing through the small gaps between the blocks. The PR blocks were 32 cm tall, 15.8 cm wide, and 10.4 cm along the direction of the beam, yielding a total of 3.23 radiation lengths.

The remaining rows of blocks were at 90° to the central ray and were staggered laterally to avoid the possibility of a particle escaping through the cracks. The rows were labeled TA, TB, TC, and TD and had seven blocks per row, except for TD which had only six. Since the majority of the shower was contained in the TA blocks, two phototubes were attached to these blocks to maximize the light collection, one on top (TAU) and one on the bottom (TAD). The blocks were made of F-5 type Pb glass, and were 40 cm tall, 14.6 cm wide, and 14.5 cm along the direction of the beam, yielding a total of 6.8 radiation lengths per row.

Two planes of scintillators were used to detect charged particles. The first plane (SF) consisted of five vertical slabs of scintillator placed between the seventh and eighth planes of wire chambers, whereas the second plane (SM) was located immediately after the PR blocks. It was comprised of three horizontally placed scintillators which had phototubes on both ends. Signals from both planes of scintillators were used as components of the trigger and as a means of identifying tracks.

A highly segmented hodoscope containing 42 thin scintillators was mounted onto the front face of the shower counter frame. The hodoscope had two planes of horizontally placed scintillators to give vertical segmentation, and two planes of vertically placed scintillators to give horizontal segmentation. All scintillators were equipped with Hamamatsu R239 phototubes operating at roughly 1800 V.

D. The 1.6 GeV spectrometer

1. Optics

The 1.6 GeV spectrometer [22] nominally consists of one 90° vertical bend dipole magnet. To increase the solid angle, two 10Q18 quadrupoles were inserted before the dipole as shown in Fig. 9. A tungsten collimator, placed at the entrance to the quadrupoles, restricted the vertical scattering angle, $\Delta\Phi$ to less that ± 120 mr. The range spanned by the differential horizontal scattering angle, $\Delta\Theta$, was ± 60 mr, and the fractional momentum, δ, ranged from -6% to $+6.8\%$ of the central value, yielding a fairly large solid angle of approximately 8 msr. Reverse matrix elements were generated from a Monte Carlo simulation of the spectrometer optics. Typical momentum and production angle resolutions obtained using the detectors were $\pm 0.2\%$ and ± 3.0 mr, respectively.

A survey of the spectrometer angle after the experiment indicated that the central axis of the dipole was $\simeq 3.2$ mr less than 90°. This misalignment between the dipole and quadrupole central axes had a slight effect on the spectrometer optics, designed to be line-to-point in the horizontal plane and point-to-point in the vertical plane, resulting in an asymmetry about the central axis in the horizontal plane as illustrated in Fig 10. A second anomaly in the optics was caused by incorrect current settings for the quadrupoles. A recalibration of the quadrupole power supplies after the experiment, indicated that the currents were less than their respective set points by 1.07% and 1.75%. This caused a shift in the production angle focal plane from the design value of 9 m to 11.5 m, and was also partially responsible for the observed spread in horizontal scattering angle as a function of particle momentum, δ.

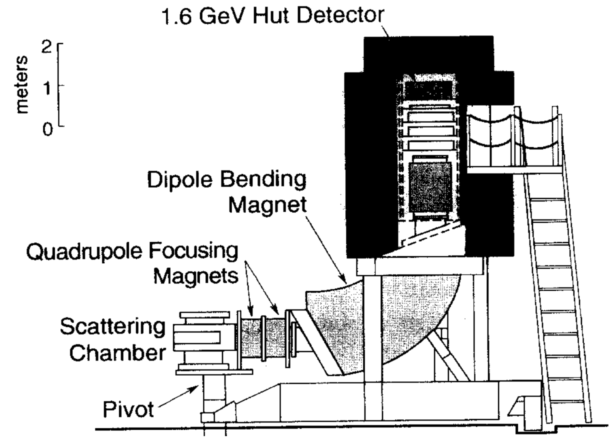

FIG. 9. The 1.6 GeV spectrometer. Two quadrupoles, Q1 and Q2, were placed prior to the 90° vertical bend dipole, B1, to increase the solid angle by a factor of three. The spectrometer remained fixed at 90°, and operated at central momenta between 0.1 – 0.8 GeV/c.

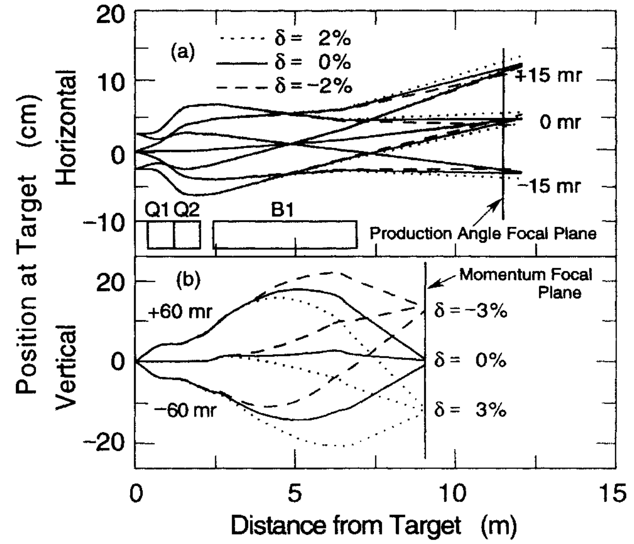

FIG. 10. The horizontal (a) and vertical (b) optics for the 1.6 GeV spectrometer. The boxes indicate the location of the magnets, Q1, Q2, and B1.

The central momentum range spanned with the inclusion of the two quadrupoles was 0.1 – 0.8 GeV/c. A precision NMR probe identical to those used for the 8 GeV magnets, was attached to the dipole magnet and measured the field in both the central and fringe field regions. Although the magnetic field was measured to within $\pm 0.01\%$, the relation between the field and the central momentum was known to only $\pm 0.3\%$ [26]. Thus, the true central momentum was determined using the elastic peak calibration method described in Appendix A.

2. Detectors

The 1.6 GeV threshold Čerenkov counter was the first detector in the detector hut, as illustrated in Fig. 11. The Čerenkov counter was 1.4 m long with 0.41 mm thick aluminum entrance and exit windows. Two mirrors served to focus the Čerenkov radiation onto the face of an RCA 8854 phototube which had been coated with a wavelength shifter. The first mirror was located 1.2 m from the entrance and was tilted at an angle of 28° to reflect the light onto a spherical mirror placed opposite the phototube. The surface of the spherical mirror was coated with MgF to prevent oxidation. A reflective cone made of aluminized Lucite was attached to the phototube to enhance the light collection. It extended 10 cm from the face of the phototube at an angle of 27°, and

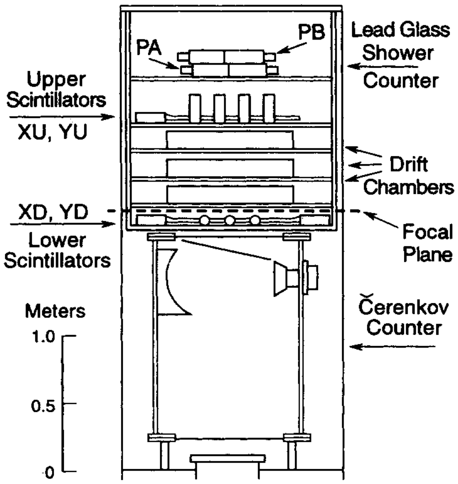

FIG. 11. The 1.6 GeV detectors. The detector package consisted of a carbon dioxide-filled threshold Čerenkov detector followed by three groups of drift chambers and a lead glass total absorption counter. Two groups of scintillators, an upper and a lower, were installed above and below the drift chambers, respectively.

effectively increased the light collection surface area by a factor of 2.5. A laser was used to align the mirrors such that the maximum amount of light was reflected into the cone.

The counter was filled with carbon dioxide gas at 760 mm Hg. An index of refraction of 1.00045 at 25 °C yielded pion and electron thresholds of 4.7 GeV and 0.017 GeV, respectively. An average of 54 photons was emitted over the length of the counter, and the probability of a pion creating a knock-on electron was negligible for pion energies less than 1 GeV.

For track determination, the 1.6 GeV spectrometer had three separate drift chambers, each consisting of four planes, two X and two Y. Field shaping and anode wires within the planes were alternately placed at 1 cm intervals. Although the anode wires were spaced 2 cm apart in each plane, adjacent planes were close enough together (0.9 cm) to be treated as one. Thus, effectively each drift chamber contained an X and Y plane with anode wires spaced 1 cm apart since the positions of the anode wires were staggered in the two planes. A total of 62 wires comprised the X plane while 42 wires comprised the Y plane, yielding an active area of 60 by 40 cm. The anode wires were 0.2 mm in diameter and were kept at a voltage of approximately 1850 V, while the field shaping wires were kept at −500 V. Thin, grounded foils of aluminized kapton separated the planes and contained a gas mixture of 89.06% argon, 9.92% carbon dioxide, and 1.02% methane which flowed continuously through the chambers at a rate of 20 cc/min.

The 1.6 GeV shower counter consisted of two slightly offset planes (PA and PB) of 14 blocks each. Each plane contained two rows of 7 blocks which were 25 cm long by 10 cm wide and 10 cm along the direction of the beam. The blocks were made of SF-6 type Pb glass which has a radiation length of 1.69 cm yielding a total of 11.8 radiation lengths for the counter. Each block was outfitted with a Hamamatsu R1911 phototube.

Two planes of scintillators, one segmented in the X direction, the other in the Y direction, were placed both before and after the drift chambers. The lower pair (XD and YD) consisted of 5 X and 3 Y scintillators, each of which had phototubes on both ends. The upper pair (XU and YU) consisted of 6 X and 4 Y scintillators. The Y plane scintillators had tubes on both ends, while the X plane scintillators had tubes on one end only. All scintillators were 11 cm wide and arranged such that their edges overlapped by roughly 1 cm. RCA 8575 phototubes were used with voltages between 1800 and 2200 V. These scintillators were used in the trigger and for track identification.

E. Trigger electronics

1. 8 GeV trigger

Raw signals from the detectors were grouped into two types, those which were components of the trigger and those which were not. The trigger signals were conducted via fast heliac cables; these included signals from the phototubes of the SF and SM scintillators, the PR and TAD blocks, and the Čerenkov counter. Signals from TAU, TB, TC and the 42 scintillators of the hodoscope were transmitted by standard coaxial cables. The delayed pulses from the hit wires in each of the chambers were retrieved via a common fast load signal which latched the delayed signals whenever the trigger fired. Figure 12 shows a schematic of the trigger components and electronics.

The 8 GeV trigger was designed to be 100% efficient

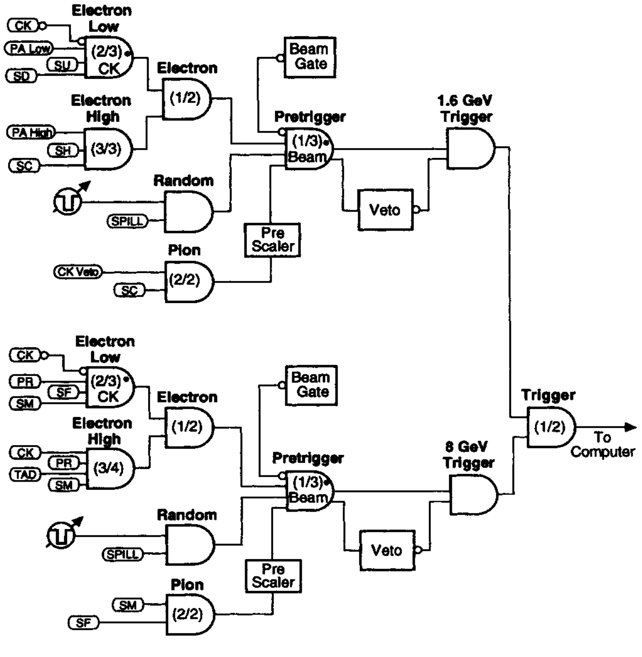

FIG. 12. Components of the trigger electronics for both the 8 GeV and the 1.6 GeV detectors.

at detecting electrons while maintaining high pion rejection. To accommodate the wide range in spectrometer momentum settings, the Electron trigger was composed of a logical OR of two components: Electron Low, which was optimized for the low E' Electron events, and Electron High which was optimized for moderate to high E' electrons. The trigger gate width was 20 ns. In addition to the Electron Trigger, two other trigger signals were defined. These were the Pion Trigger used to collect a sample of pion events, and a Random Trigger, the function of which was to monitor the analogue-to-digital converter (ADC) pedestals. A Pretrigger was formed which required one out of the three primary trigger signals in coincidence with a beam gate. The output from the Pretrigger was sent to the main 8 GeV trigger, which was set to accept only one event per beam pulse since the computer was incapable of handling more. Derived from the 8 GeV trigger signal were gates to the ADC's, starts for the time-to-digital converters (TDC's), gates for the latches, an interrupt to the computer instructing it to log all the event information to tape, and the fast load signal needed to latch the wire chamber information.

The Electron-High Trigger required a 3 out of 4 coincidence between the Čerenkov, the PR summed signal, the TAD summed signal, and the SM signal. Since each of these was highly efficient for electrons, and the Čerenkov and lead glass had good pion rejection capabilities, this trigger was efficient and selective. However, at low E' it was possible for the electron shower to be completely contained within the PR blocks thus effectively reducing the efficiency of Electron-High to a 3 out of 3 coincidence between the Čerenkov, PR and SM signals. To compensate for the resulting decrease in efficiency at low E', the Electron-Low trigger only required 2 out of 3 signals between the PR blocks, SF, and SM, in coincidence with the Čerenkov counter. By requiring that the Čerenkov counter fire, pion contamination was kept at a minimum. The inclusion of SF instead of TAD increased the electron efficiency at low E'.

The Pion Trigger was formed by the coincidence of the SF and SM scintillators. Since this had a high efficiency for any charged particle, the output was sent to a prescaler which reduced the raw rates by 2^8 to 2^{11}. The pion sample generated by this trigger was used to study the response of the Čerenkov and lead glass detectors to pions.

In addition to the primary trigger electronics, several parallel coincidence circuits were maintained in order to determine the electronic and computer dead-times. A set of three circuits was formed using coincidences identical to the Electron Trigger, but with gate widths of 40, 60, and 80 ns, respectively. A similar set of four circuits, denoted PTC, was formed by the coincidence of signals from the PR and TAD blocks and the Čerenkov counter. Gate widths of 20, 40, 60, and 80 ns were produced. Rates for each circuit were accumulated by scalers.

2. 1.6 GeV trigger

The trigger electronics associated with the 1.6 GeV detectors were similar to those configured for the 8 GeV triggers. The Electron Trigger consisted of the logical OR between two components, Electron-Low and Electron-High as illustrated in Fig. 12. The Electron-High required a 3 out of 3 coincidence between PA-High, SC, and SH, where PA-High indicates that the summed signal from the PA blocks was above a high discriminator threshold of 550 mV, SC indicates that at least three out of four of the scintillator planes (XU, YU, XD, YD) fired, and SH indicates that the summed signal from all PA and PB blocks was above a discriminator threshold of 750 mV. The Electron-Low trigger required the Čerenkov to fire above the 100 mV threshold, as well as a 2 out of 3 coincidence between PA-Low, SU, and SD, where PA-Low indicates that the summed signal from all PA blocks was above a low discriminator threshold of 280 mV, SU indicates that both the upper (XU and YU) planes of scintillators fired, and SD indicates that both lower (XD and YD) planes of scintillators fired. The Pretrigger was identical to that of the 8 GeV, requiring one out of either the Random, Pion, or Electron Triggers, in coincidence with a beam gate. The Pion Trigger required a coincidence between the Čerenkov veto (ČV) and SC. Dead-time coincidence circuits similar to those of the 8 GeV were constructed requiring coincidences between the Čerenkov detector and the PA and PB blocks.

F. Data acquisition

The main source of computing power was a Vax 11-780, which was responsible for monitoring the experiment, storing the data on magnetic tape, and performing an online analysis of a sample of the data. Two additional computers, a PDP-11 and a MicroVax II, were used to perform specific dedicated tasks. The PDP-11 read in the hardware ADC, TDC, scaler, and latch information for each event using a Jorway Branch Driver, and stored it in a large buffer within the Vax memory. The MicroVax II was used to control the beam steering and read the toroids. Periodically it transferred this information to the Vax.

The data were written to magnetic tape in units of "runs" which typically corresponded to 1 h of data-taking. Data runs were broken down into "checkpoints" which marked 3-min intervals of real time.

III. DATA ANALYSIS

The first step of the analysis procedure was to remove faulty data. Data reduction then proceeded with an event-by-event analysis, in which the Čerenkov detectors and lead glass shower counters were used to identify electrons from background pions, while wire chambers were used to reconstruct particle trajectories. Reverse matrix elements for each spectrometer were used to extrapolate the trajectory coordinates to the corresponding target scattering angle and momentum. Corrections to the data were made for detector inefficiencies, electronic and computer dead-time, fluctuations in target density, incident charge, and kinematic quantities. Corrections were also applied to account for radiative processes of higher order than the single-photon approximation assumed in the derivation of the Rosenbluth formula.

A. Bad data elimination

Faulty data were associated with a hardware failure or error while taking data. For example, when a run was ended abruptly due to the sudden loss of beam or of a magnet power supply, data accumulated after the last checkpoint was usually faulty and was therefore discarded. However data were also eliminated according to the following criteria.

(1) When quadrupole currents strayed from their set points by more than 0.5 A, or 0.6 A if the set point was greater than 600 A, thereby causing greater than ±0.5% variation in the spectrometer acceptance. Similar criteria were not imposed on the dipole magnets since slight fluctuations in dipole current could be corrected for using the accurate NMR readings logged to tape every ten seconds.

(2) When any event counter (scaler) fluctuated between two checkpoints by more than twice its average value over the data run. However, due to noisy wire conditions, checkpoints were discarded based on the 1.6 GeV wire chamber scalers only if fluctuations were observed which were five times greater than the average values over the run.

(3) When the overflow or underflow bins of the ADC histograms associated with the toroids, wire arrays, and microwave cavity contained significant contributions compared with the total ADC spectrum. Contributions in these bins were indicative of charge readout and beam steering problems.

B. Event analysis

1. *Particle identification*

The combination of information provided by the lead glass and Čerenkov counters provided a highly efficient means of separating electrons from background pions. In the shower counters, a normalized shower energy, defined by the ratio of energy deposited in the shower counter to momentum of the particle track, was determined by summing the pedestal-subtracted ADC pulse height signals from each block which contained a portion of the shower for a given event as determined by the particle track. To add signals from different blocks together, each block was calibrated such that the normalized shower energy spectrum of an electron would be peaked at unity when divided by the momentum. Calibration coefficients were determined from a least squares fit which minimized the shower energy spectra widths generated for a clean sample of electron events. For the 8 GeV shower counter, the calibration also included effects due to attenuation of the Čerenkov light along the length of the lead glass block. No such dependence on particle position was found for the 1.6 GeV lead glass blocks within the fiducial region. The energy resolutions were $\pm 8\%/\sqrt{E'}$ and $\pm 5\%/\sqrt{E'}$ for the 8 GeV and 1.6 GeV counters, respectively, in good agreement with the expected values for the lead glass used in each counter.

For a particle to be considered an electron, it had to satisfy software cuts in both the shower counters and the Čerenkov detectors. For the shower counters, the normalized shower energy was required to be above 0.7 and 0.6 in the 8 GeV and 1.6 GeV spectrometers, respectively. These cuts were chosen to maximize both electron detection and pion rejection, and yielded efficiencies of 99.4% and 98.0% for the 8 GeV and 1.6 GeV counters, respectively. The 1.6 GeV Čerenkov ADC was required to be above channel 25, a cut slightly above the hardware threshold, yielding a detector efficiency of 99.9%. In the 8 GeV counter, the nitrogen gas was scintillating [27] and producing a small signal at the one-photoelectron peak for the higher π/e runs, as shown within the circle in Fig. 13. To eliminate these background events (mostly pions) the software cut was placed at channel 50, thereby incurring an electron inefficiency of roughly 1%. A Poisson fit to typical ADC spectra indicated an average of 6.8 photoelectrons produced in the 8 GeV detector and 7.8 in the 1.6 GeV detector, values consistent with phototube quantum efficiencies of approximately 13%.

To illustrate the electron–pion separation achieved by requiring both the Čerenkov and shower counter signals to be above their respective cuts, we can compare the normalized shower energy spectra for events which *did* and *did not* produce a signal above the Čerenkov cut. In Fig. 14, plots (a) and (c) show the normalized shower energy spectra for all events which fired either the electron or pion triggers, whose reconstructed quantities were con-

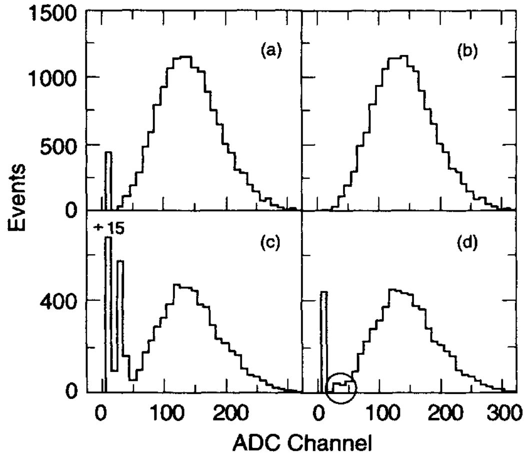

FIG. 13. 8 GeV Čerenkov spectra. The upper plots (a) and (b) show typical hydrogen elastic spectra. In (a) no cut was required on the shower energy, while in (b) the shower energy was required to be above the electron cut of 0.7. Figures (c) and (d) show similar spectra but for a high π/e run where the nitrogen gas was scintillating. Although requiring a cut on normalized shower energy (d) reduced the pion background, a small bump remained at the one-photoelectron peak, shown within the circle, necessitating the Čerenkov cut be placed at channel 50.

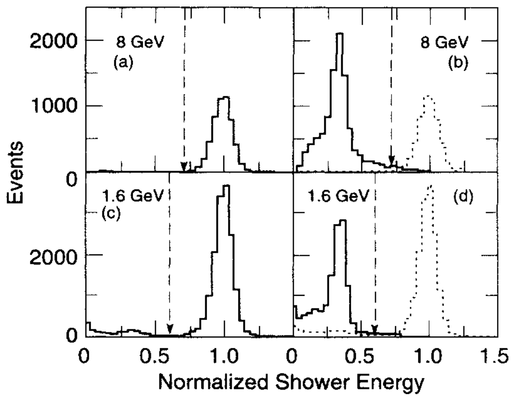

FIG. 14. Normalized shower energy spectra. Plots (a) and (c) correspond to electron spectra for which the Čerenkov detectors were required to fire, in the 8 and 1.6 GeV shower counters, respectively. Plots (b) and (d) illustrate the pion spectra for which the Čerenkov did not fire, given by the solid histogram. The dotted histogram gives the electron spectra of (a) and (c) for comparison. The dashed arrows indicate the cut above which events were deemed electrons.

sistent with particles originating at the target, which produced only one good track, and which fired the Čerenkov detector above the 8 GeV and 1.6 GeV respective cuts. The peaks are centered at unity, indicating most of the events were electrons. The arrows correspond to the software shower energy cuts above which events were counted as electrons. For comparison, the solid histograms in plots (b) and (d) correspond to normalized shower energy spectra for events from the same run, but for which the Čerenkov detector *did not* fire above the cut, and therefore correspond to background pion events. The electron spectra of plots (a) and (c) have been superimposed (dotted histograms) to illustrate the clear separation between electron and pion events.

Although the electron and pion spectra are clearly separated, the tail regions of each spectrum must be addressed. The tails of the pion spectra above the shower energy electron cut were used to determine the fraction of events which were deemed electrons, but which were actually pions. These events amounted to a small correction to the electron sample, discussed in detail below. The tails of the electron spectra below the shower energy cut represent the inefficiency of the shower counters. Note that the tail was fairly significant for the 1.6 GeV counter which is reflected by the slightly low efficiency of 98.0%. It was determined that the events which comprised the tail were electrons whose total shower energy was not contained within the lead glass, thus the normalized shower sum was less than unity for those events. The missing shower energy was either lost between the cracks of adjacent blocks, or lost out the back of the counter, which was 11.8 r.l. long.

2. Particle tracking in the 8 GeV spectrometer

The method for finding the correct particle track associated with each event consisted of three principal stages: grouping the hit wires, searching all possible pairs of hit wires for tracks, and in the case of multiple tracks per trigger, purging those which were spurious. The few events for which no track could be found were attributed to the inefficiency of the chambers.

Adjacent hit wires which formed a group were further broken down to contain a maximum of only two hit wires. By limiting the group size to no more than two adjacent wires, greater tracking resolution was achieved. The centroid of each group was randomized over ±0.5 wire spacing to give a smooth distribution of hit positions.

The tracking routine then searched for all possible trajectories between each group of hit wires. It first tried to find tracks requiring a minimum of seven chambers with signals per track, three of which had to be P chambers and three of which had to be Θ chambers. If no track was found it tried again reducing the requirement to only six chambers per track, but insisting that two P and two Θ chambers fired. Finally, if still no track was found the routine tried one last time reducing the number of chambers per track to five, but still requiring that two P and two Θ had fired. The procedure was to first find a track using the P chambers and if successful, look for a track using the Θ chambers.

The algorithm was the same for P and Θ chambers, and will be described here for the P chambers. All possible pairs of groups between a pair of chambers were considered. Trajectories defined by each pair of hit wires were extrapolated or interpolated to determine which wires should have fired in the remaining three P chambers. A search was then made on these three chambers to see if the required wires fired. A margin of ±2 wire spacings was allowed in searching for the possible hit wire. If the minimum number of P chambers required was found with hits on the track, then the hit positions were fit with a line to extract the slope and intercept. The same procedure was then applied for the Θ chambers. The entire process was continued until all groups of hit wires between pairs of chambers were considered.

For approximately 3% of the events from the hydrogen target, more than one track was found and it was necessary to purge any additional tracks so that only one track was retained. The criterion was to select the track corresponding most closely to a good electron event, unless a pion trigger fired. In the latter case we sought to retain pions by *not* purging tracks with a normalized shower energy less than 0.7. This eliminated tracks for electrons in coincidence with a pion trigger, which were already accounted for by the one-per-pulse dead-time correction. The hierarchy of conditions used to eliminate tracks was as follows: (i) the normalized shower energy was less than 0.7 (only for electron triggers), or the track pointed to the edge region of the shower counter array; (ii) failure of the trajectory to extrapolate back to the target; and (iii) lack of signals on both scintillator planes in the hodoscope. If more than one track still remained, then that with the least number of struck chambers was purged, or if equivalent, then that with the worst χ^2 from the fit to hit positions. The efficiencies of individual chambers ranged from 95 to 98%, and the overall tracking efficiency was 99.9%, except for SLED runs for which it

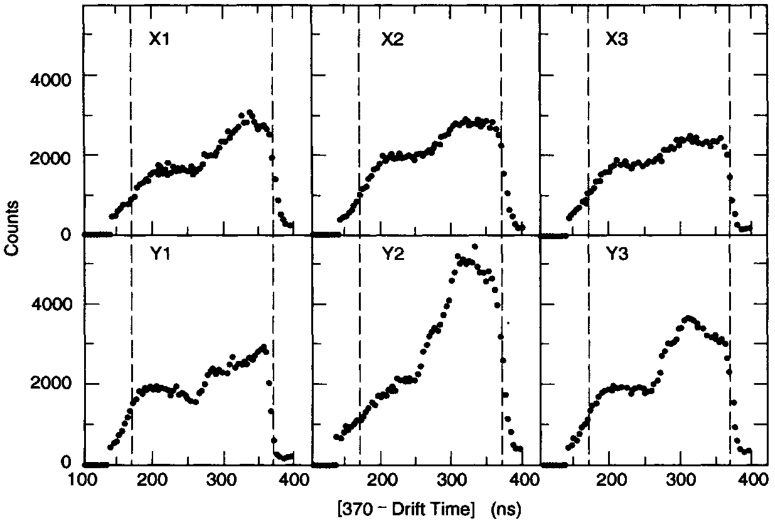

FIG. 15. 1.6 GeV drift time spectra summed over all wires per chamber for one run. The dashed vertical lines correspond to drift distances of 1.0 cm (left side) and 0 cm (right side). The "two step" distributions, instead of the expected square wave forms, indicate that the drift velocities were nonuniform and tended to be larger in the 0.5 cm close to the anode wires.

was 99.7% due to higher singles rates which increased the wire dead-times.

3. Particle tracking in the 1.6 GeV spectrometer

The 1.6 GeV tracking procedure was complicated due to intermittently noisy wires (mostly cross talk between adjacent wires) which degraded the chamber performance during certain periods of the experiment. To overcome this problem, a careful study was made of the cross talk problem and the tracking algorithm was designed to not use likely cross talk events if a cleaner event was available. Scintillator masking was also utilized such that only wires within a geometrical range allowed by the scintillators which fired were included in the tracking algorithm. If this produced no tracks for a given event then the masking was turned off and the tracking algorithm was tried again.

The TDC information from each wire was first converted to a drift time using TDC calibration data. Figure 15 shows sample drift time spectra summed over all wires in each chamber for a given run. Ideally, these spectra should have a uniform distribution corresponding to a constant drift velocity of 0.005 cm/ns. The two-step distribution indicates a slightly faster drift velocity near the wires. For adjacent wires which fired, the sum time was given by the sum of the drift times for each wire of the pair. Figure 16 shows sum time spectra calculated from all pairs of adjacent firing wires in each drift chamber. A good sum time was defined to be one which was within reasonable limits of the ideal sum time of 200 ns corresponding to 1 cm wire spacing. A hit position was determined by averaging the two drift times which were converted to drift distances. Problems due to the slight nonlinearity of the drift velocities tended to cancel when this average was taken. The position resolutions in each chamber varied for good sum time events between ±0.7 and ±1.5 mm. If a single wire fired it was considered a hit only if no good sum time pairs could be found. Since it was not possible to determine which side of the wire an event occurred, the hit position was defined to be the

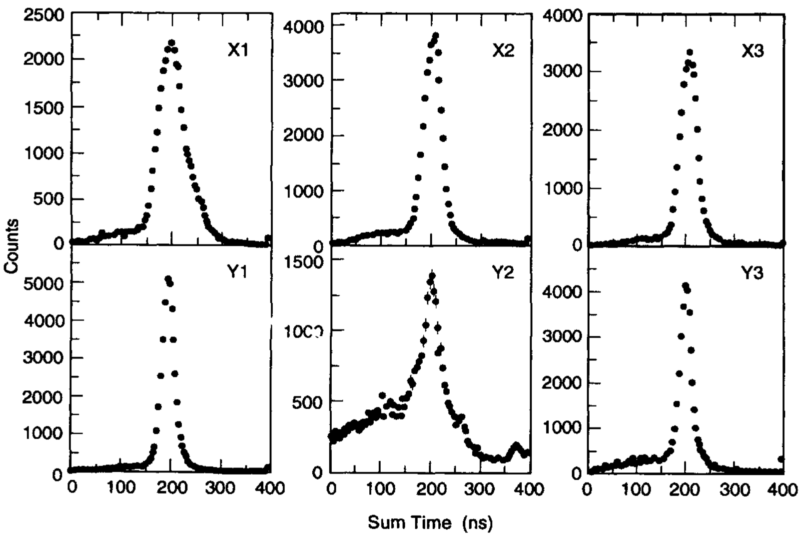

FIG. 16. 1.6 GeV sum-time spectra for all pairs of adjacent wires which fired per chamber for one run. A peak was formed at the expected sum time of 200 ns, corresponding to the nominal total drift time between two wires. This run illustrates a worst case example of the cross talk problem in Y2, indicated by the relatively poor sum-time peak.

wire position with a total error of twice the calculated drift distance.

Once all the hit positions were defined, the tracking algorithm calculated the likely track candidates in both X and Y. In the case of multiple tracks, purging was done in a manner similar to that of the 8 GeV tracking with one notable exception. Scintillator hit positions were calculated for scintillators having a phototube at each end using their timing information. The resolution was $\sim 2-4$ cm. Tracks pointing more than 2.0 cm from a scintillator hit position were purged. The overall tracking efficiency was 99.3%.

4. *Electron definitions and histogramming*

The software definition of an electron was more restrictive than the hardware electron triggers which were designed to be 100% efficient for electrons while also accepting some fraction of background. Two software definitions ELECT1 and ELECT2,were constructed for electrons in each spectrometer. ELECT1 was the primary definition used to obtain the final cross sections, while ELECT2 was used as a means of checking the efficiency corrections. Pion events were also defined in two ways PION1 and PION2 for each spectrometer as described in Ref. [15].

The ELECT1 definitions for both spectrometers required that an event: (i) fire either the electron or the pion trigger; (ii) have at least one good track (TRACK); (iii) have a normalized shower energy above the software cut (SHWR); (iv) have a Čerenkov signal above the software cut (CKADC), effectively eliminating any contribution from the pion trigger; and (v) have reconstructed δ, $\Delta\Theta$, and $\Delta\Phi$ values which came from the target region (RECON). In addition to these requirements, the 8 GeV ELECT1 definition required trajectories to lie within the good fiducial region of the spectrometer acceptance (GOODFID), a region defined to be the area of the face of the PR blocks except the region less than 3.5 cm from the edges.

The ELECT2 definitions were more restrictive, including the extra requirement that an event have a reconstructed horizontal position (TARGX) within limits of the target region. In addition, the 1.6 GeV ELECT2 definition placed a more restrictive cut on the normalized shower energy (SHWR2) of 0.75 as opposed to 0.6 used for ELECT1.

Electron and pion events were accumulated in two-dimensional arrays according to their reconstructed $\Delta P/P$ and $\Delta\Theta$ values, thereby integrating over $\Delta\Phi$. To ensure that the resulting cross sections were independent of $\Delta\Phi$, four histograms were accumulated for each spectrometer corresponding to the following $\Delta\Phi$ ranges: ± 28 mr, ± 24 mr, ± 20 mr, and ± 10 mr for the 8 GeV spectrometer, and ± 120 mr, ± 100 mr, ± 80 mr, and ± 60 mr for the 1.6 GeV spectrometer. A total of ten event histograms were stored for each spectrometer, five for electrons denoted $N(\Delta P, \Delta\Theta)_{i,e}$, and five for pions denoted $P(\Delta P, \Delta\Theta)_{i,\pi}$, where the index i runs from 1 to 5. In addition to the four $\Delta\Phi$ versions, the fifth histogram was stored for the largest $\Delta\Phi$ cut, but for events which satisfied the second particle definition, either ELECT2 or PION2.

The ranges and bin widths were chosen to cover the full acceptance of each spectrometer, including the edge regions, and to minimize the uncertainty in W^2 by making the bin width as small as possible, yet still large enough to retain good statistics.

C. Corrections to the data

1. *Detector inefficiencies*

A single correction factor EFF_{corr} was applied to the cross section in order to account for detector inefficiencies. This factor was equal to the product of the efficiencies of the various elements contributing to the electron definitions, except for the geometrical cuts GOODFID and RECON, neither of which contributed to the inefficiency since both were required when generating the acceptance functions. Because of the momentum-dependent effects of multiple scattering in the 8 GeV spectrometer, the efficiency for TARGX exhibited a slight dependence on E', determined from Monte Carlo acceptance simulations as a function of E'. The efficiencies for the various requirements and for ELECT1 and ELECT2 are summarized in Table II. The uncertainties in EFF_{corr} were estimated at $\pm 0.2\%$ for the 8 GeV detectors, and $\pm 0.3\%$ for the 1.6 GeV detectors based on the level of agreement obtained between cross sections determined using the two electron definitions.

2. *Electronic and computer dead time*

Corrections were made to the cross section to account for events which were lost due to electronic and computer dead time. The total dead-time correction D_{corr} was given by product of the two. Electronic dead time was due to the 20 ns width of the primary trigger gate. Once an event fired the trigger, the electronics were unable to accept any additional events for the duration of the trigger gate. To correct for the electronic dead time, scaler rates corresponding to triggers formed with 40, 60,

TABLE II. Detector efficiencies. The efficiencies of ELECT1 and ELECT2 are determined by the product of the efficiencies of the requirements of which they are comprised.

8 GeV		1.6 GeV	
Requirement	Efficiency	Requirement	Efficiency
CKADC	0.990	CKADC	0.999
SHWR	0.994	SHWR	0.980
TRACK	0.999 (0.997 SLED)	SHWR2	0.970
TARGX	$1.0 - \frac{0.0005}{(E')^2}$	TRACK	0.993
		TARGX	0.956
Particle Def.	E_{corr}	Particle Def.	E_{corr}
ELECT1	0.983 (0.981 SLED)	ELECT1	0.972
ELECT2	ELECT1$\cdot(1.0 - \frac{0.0005}{(E')^2})$	ELECT2	0.920

and 80 ns gate widths were linearly extrapolated to that of an ideal trigger width of 0 ns. For the SLED runs the trigger gate widths were reduced to 30, 40, and 50 ns, respectively, since the beam pulse width was only 150 ns. For most hydrogen runs, the electronic dead-time correction was less than 0.2%, but for a few runs it was as large as 1.0%.

The computer was capable of processing only one event per beam pulse. Thus, once an event occurred, the computer was effectively dead to any events occurring during the remainder of the beam pulse. Since the pulse width was 2 μs, the computer dead time could be much larger than the electronic dead time. The computer dead-time correction was obtained by taking the ratio of scaler rates for the PTC coincidence circuits to their veto equivalent circuits, PTCVETO. In the veto circuits, the scalers stopped counting after the first trigger within the beam pulse, while for the nonveto coincidences, the scalers counted all events within the beam pulse. The computer dead-time correction ranged from 0.2% to 14% for hydrogen targets.

An alternative method of determining the total dead time is to use Poisson statistics which give the probability of observing n events within the beam spill as

$$P(n,\mu) = \frac{\mu^n}{n!}e^{-\mu}, \tag{15}$$

where μ is the mean number of events per beam spill. The correction is given by

$$D_{\text{corr}} = \frac{\mu}{1 - e^{-\mu}}. \tag{16}$$

Both methods, Poisson statistics and scaler rates, should yield the same results within errors given the relatively constant luminosity of this experiment. Figure 17 shows the dead-time corrections calculated by the two methods plotted against one another for the hydrogen targets. With the exception of the SLED runs, the two methods agreed within ±0.2%. For the SLED runs, however, a systematically larger result was obtained from the Poisson method compared to the scaler method, with a difference up to 1.5%. In this case we relied upon the Poisson result, since the scaler method became less reliable for the narrower beam pulse of the SLED runs, and the Poisson method did not depend on the beam pulse length. An uncertainty of ±0.2% was assigned to the dead-time correction based on the level of agreement found between the two methods of calculation.

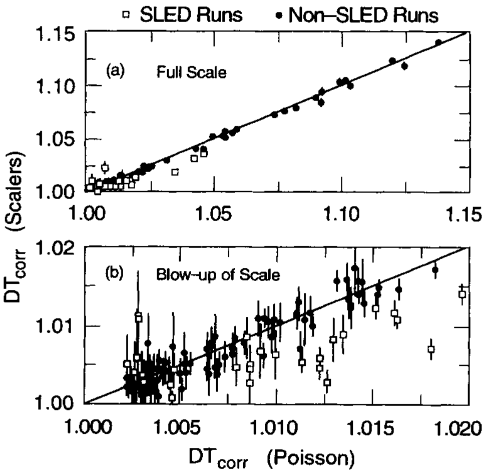

FIG. 17. The dead-time correction, D_{corr}, calculated from event scalers plotted versus that calculated from Poisson statistics.

3. Kinematic calibration

The spectrometer central scattering angles, Θ_8 and $\Theta_{1.6}$ were surveyed both before and after the experiment. The 8 GeV survey indicated a variation in the measurements consistent with ±0.006°. The nominal angle for each run was corrected according to the survey values. The post experimental survey of the 1.6 GeV indicated that the dipole magnet was tilted relative to the vertical axis, with the net effect that the dipole central axis was at a smaller scattering angle than the central axis of the quadrupoles by 0.183°, and imaged a spot 4 mm upstream of the target center. The quadrupole central axis was surveyed at 90.000° to the beam line, and therefore the dipole was at 89.817°. An uncertainty of ±0.05° was ascribed to the 1.6 GeV scattering angle.

The central momentum of the spectrometers was determined from magnetic field measurements obtained with precision NMR probes. For the 8 GeV spectrometer, the central momentum, E'_8, was obtained for each run from the relation [24]

$$E'_8 = (0.41512\ B + 0.00050) - \delta E'_{8,\text{shift}}, \tag{17}$$

where B (kG) was the average of the magnetic fields measured in the dipoles. The term in parentheses, the characteristic equation relating E'_8 and B, was well determined by the floating-wire calibration [24] of the spectrometer. The second term $\delta E'_{8,\text{shift}}$ accounted for a small shift needed to center the elastic peaks based on the calibration procedure described in Appendix A. The size of the shift was a function of spectrometer momentum and ranged from 0.07% at 0.5 GeV to 0.01% at 8 GeV.

The 1.6 GeV central momentum, $E'_{1.6}$, was given by

$$E'_{1.6} = (0.07500\ B + 0.00024) - \delta E'_{1.6,\text{shift}}. \tag{18}$$

Unlike the situation in the 8 GeV, the characteristic equation was not as well known, particularly with the addition of the two quadrupoles. The elastic peak calibration indicated that a shift of 0.14% was needed to center the peaks.

The incident electron energy E was measured using the flip coil located in the A bend. The results of the elastic peak calibration showed the need for a shift in E of 0.04% in order to obtain the best χ^2. Thus,

$$E = E_{A\ \text{bend}}(1 + 0.0004). \tag{19}$$

In addition to this systematic shift, the energy of several runs was adjusted within an estimated point-to-point uncertainty of ±0.06% based on the residual scatter in peak positions. An overall systematic uncertainty of ±0.05% was assigned to E which is about a factor of 2 smaller than previous ESA experiments. This error was limited due to the precision with which E'_8 and Θ_8 were measured, and was supported by the small shift of only 0.04% needed to center the elastic peaks.

Because of ionization losses as the electron passed through the target and scattering chamber material, the true incident and scattered energies of the electron at the interaction vertex were generally slightly different from their respective measured values. The most probable energy loss depended on the kinematics and the target geometry, and was typically 2 MeV before the scattering point, and 1.4 MeV after scattering.

4. *Background subtractions*

Corrections to the elastic cross sections were made for two sources of background contamination. These were pions misidentified as electrons, and electrons which scattered from the aluminum end caps of the target rather than the hydrogen. An additional background due to pair production ($\pi^o \rightarrow \gamma\gamma \rightarrow e^+e^-$) was measured by reversing the polarity of the magnets to detect positrons. This background was found to be negligible for elastic scattering from hydrogen.

a. Pion subtraction. Background pions contaminated the electron sample by producing hadronic showers in the lead glass with a normalized shower energy above the electron cut, and simultaneously causing the Čerenkov to fire either by creating a knock-on electron or by having a momentum greater than the pion threshold. The size of the pion contamination was determined using the normalized shower energy distribution of pions shown in Figs. 14(b) and (d). From the shape of the distribution we calculated the fraction of pions with shower energies above the electron cut. This fraction was multiplied by the fraction of pions which gave signals in the Čerenkov counter. The latter factor was estimated by taking the ratio of the number of electrons (shown by the dotted histogram) in a region about the pion peak, to the number of pions in the same region. The pion subtraction was done for both hydrogen and aluminum targets. For the elastic hydrogen data the correction was very small, typically less than 0.01%, and always less than 0.08%. For the aluminum targets, the correction was as large as 3.5%. The uncertainty in the cross section due to the pion subtraction was negligible.

b. Aluminum end-cap subtraction. This correction was only necessary for the 8 GeV data since for the 1.6 GeV spectrometer, electrons scattering from the end caps were blocked by tungsten bars. The end-cap correction was made by subtracting from the hydrogen data a fraction of the events measured using the aluminum dummy target normalized according to the ratio of the relative thicknesses of aluminum in the hydrogen and dummy targets. To check the validity of the aluminum end-cap subtraction, data were also taken at identical kinematics using the 4 cm targets, for which the relative size of the aluminum contribution to the cross section was much larger. Cross section results for the two targets agreed within errors, and the number of events in the "superelastic" region ($W^2 < M_p^2$) were consistent with zero. The size of the aluminum subtraction averaged over W^2, ranged from 0.8% to 4% for the higher-energy runs. An estimated uncertainty of ±0.2% was assigned to the subtraction.

5. *Radiative corrections*

Radiative correction procedures [28,29] relate the single photon exchange cross section $\frac{d\sigma}{d\Omega}$ to the measured raw cross section as follows:

$$\frac{d\sigma}{d\Omega}_{\rm raw} = R_{\rm corr}\left(\frac{d\sigma}{d\Omega}\right), \tag{20}$$

where the factor $R_{\rm corr} \equiv e^{\delta_{\rm corr}}$, $\delta_{\rm corr} = (\delta_{\rm int} + \delta'_{\rm int} + \delta_{\rm ext})$, and $\delta_{\rm int}$ and $\delta_{\rm ext}$ parametrize the internal and external radiative corrections. The term $\delta'_{\rm int}$ results from improvements and corrections made to the internal radiative term as described in Ref. [6].

The internal corrections include the processes of vacuum polarization, electron and proton vertex corrections, two-photon exchange, and internal bremsstrahlung, as illustrated in Fig. 18. Radiative corrections were calculated for each set of kinematics up to the specified W^2 cutoff. The size of the correction $R_{\rm corr}$ ranged from 0.71 to 0.81 for the 8 GeV cross sections and 0.81 to 0.85 for the 1.6 GeV cross sections. Table III gives the values of each component as well as the total for each set of kinematics. In order to check the external radiative corrections, a 4% radiator was inserted just upstream of the target assembly for three kinematic settings. Cross sections from each of these points agreed within errors with results from identical runs without the radiator.

The sensitivity of the external corrections on the input parameters was investigated by varying the parameters within plausible limits. The effects on the resultant

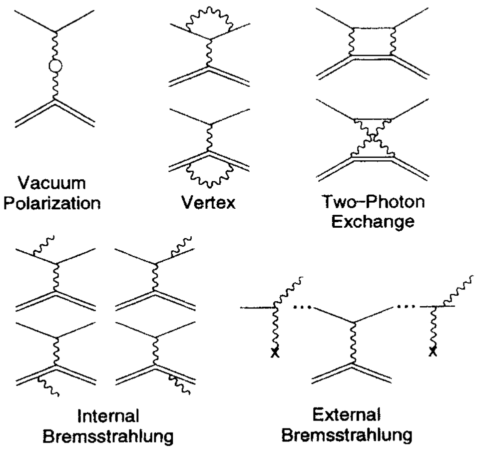

FIG. 18. Feynman diagrams included in the internal and external radiative correction calculations.

form factors were found to be much smaller than the corresponding statistical errors. The point-to-point uncertainty in the radiative corrections was estimated at ±0.5%, consistent with the cross checks just discussed. The absolute uncertainty was estimated at ±1.0%. The largest sources for this error were the exclusion of the nondivergent two-photon exchange contributions [29,30] and the approximation of higher-order effects via exponentiation of δ_{corr}.

D. Spectrometer acceptance

Acceptance functions for both spectrometers were generated by Monte Carlo simulations of the respective spectrometer optics including effects due to multiple scattering, dependence on target length, and various physical apertures and software cuts. The 8 GeV acceptance function was very well determined. The Monte Carlo simulation was based on matrix elements measured in the floating-wire calibration [24], and precise survey data for the magnets. The uncertainty in the E' and θ dependence of the acceptance was estimated at ±0.5% based on numerous cross checks, while the uncertainty in overall normalization was ±1% from the wire float calibration.

The 1.6 GeV acceptance function was more difficult to determine since a set of matrix elements did not exist for the spectrometer configuration including the two quadrupoles. By modeling the low field settings in the quadrupoles, the fringe field region of the dipole, and the misalignment between the dipole and quadrupole central axes, a ray trace program generated rays which were fit to determine the reverse matrix elements. An uncertainty of ±0.75% was estimated in the E' and θ dependence based on the comparisons and cross checks made as described below. Although the shape of the acceptance function was well known, the uncertainty in magnitude was ±5%. For this reason, the 1.6 GeV cross sections were normalized to the 8 GeV data, and therefore the uncertainty in

TABLE III. Radiative correction factors. The factors t_i and t_f refer to the number of radiation lengths before and after the scattering interaction, respectively. Note that the kinematic values listed differ slightly from those for which the cross sections are reported in Table IV. This is due to the fact that the radiative corrections were calculated for the kinematics of each point, prior to converting to the nominal set of kinematics.

E (GeV)	Θ (degrees)	W^2_{cutoff} $(\text{GeV}/c)^2$	t_i %	t_f %	δ_{int}	δ'_{int}	δ_{ext}	R_{corr}
			8 GeV spectra					
1.509	90.016	0.960	0.93	1.05	−0.1788	0.0232	−0.0713	0.7970
2.401	41.110	1.010	0.93	1.19	−0.1765	0.0225	−0.0802	0.7913
5.503	15.178	1.153	0.93	1.43	−0.1813	0.0212	−0.0957	0.7744
1.967	90.023	0.991	0.93	1.05	−0.1778	0.0302	−0.0651	0.8084
2.403	58.887	1.011	0.93	1.08	−0.1813	0.0277	−0.0709	0.7989
2.833	45.000	1.030	0.93	1.16	−0.1836	0.0265	−0.0769	0.7914
3.398	34.703	1.070	0.93	1.25	−0.1791	0.0265	−0.0804	0.7922
3.950	28.418	1.099	0.93	1.33	−0.1794	0.0261	−0.0848	0.7882
5.500	19.020	1.153	0.93	1.45	−0.1873	0.0245	−0.0950	0.7728
2.835	61.224	1.032	0.93	1.08	−0.1866	0.0316	−0.0685	0.7997
3.401	44.487	1.069	0.93	1.16	−0.1837	0.0305	−0.0736	0.7971
3.950	35.394	1.100	0.93	1.25	−0.1832	0.0297	−0.0785	0.7930
5.506	22.851	1.153	0.93	1.41	−0.1919	0.0273	−0.0917	0.7739
3.397	57.583	1.069	0.93	1.09	−0.1861	0.0355	−0.0662	0.8051
3.950	43.710	1.100	0.93	1.17	−0.1866	0.0335	−0.072	0.7982
4.507	35.603	1.131	0.93	1.25	−0.1864	0.0325	−0.0771	0.7938
5.508	26.880	1.149	0.93	1.36	−0.1968	0.0298	−0.0881	0.7749
9.804	13.261	1.141	0.93	1.38	−0.2429	0.0242	−0.1125	0.7180
3.950	59.304	1.103	0.93	1.08	−0.1877	0.0406	−0.0628	0.8107
4.508	45.657	1.131	0.93	1.16	−0.1898	0.0375	−0.0695	0.8011
5.507	32.898	1.150	0.93	1.28	−0.2007	0.0333	−0.0820	0.7793
9.798	15.377	1.146	0.93	1.44	−0.2469	0.0262	−0.1139	0.7157
9.801	17.523	1.148	0.93	1.46	−0.2512	0.0280	−0.1137	0.7140
9.806	19.763	1.146	0.93	1.45	−0.2561	0.0295	−0.1122	0.7126
			1.6 GeV spectra					
1.509	90.000	0.959	0.94	0.56	−0.1794	0.0231	−0.0498	0.8138
1.967	90.000	0.990	0.94	0.56	−0.1786	0.0300	−0.0443	0.8247
2.403	90.000	1.010	0.94	0.56	−0.1845	0.0346	−0.0421	0.8253
2.835	90.000	1.029	0.94	0.56	−0.1897	0.0388	−0.0403	0.8260
3.398	90.000	1.072	0.94	0.56	−0.1855	0.0476	−0.0348	0.8414
3.950	90.000	1.101	0.94	0.56	−0.1884	0.0536	−0.0321	0.8463
4.508	90.000	1.134	0.94	0.56	−0.1892	0.0604	−0.0289	0.8540
5.507	90.000	1.155	0.94	0.56	−0.2035	0.0649	−0.0287	0.8459

magnitude did not enter into the cross sections.

Since the acceptance functions were not determined from the data set, comparisons with the data were carried out to ensure that the angular and momentum dependencies of the acceptance functions were well understood. Figures 19 and 20 illustrate checks on the $\Delta\Phi$ and $\Delta\Theta$ dependence to the 8 GeV acceptance function, respectively. Both figures are consistent with no observed $\Delta\Phi$ or $\Delta\Theta$ dependence within the errors, indicating that the 8 GeV acceptance function was well modeled. Similar tests performed for the 1.6 GeV acceptance function, discussed in Refs. [16,17], support that the shape of the acceptance was modeled within ±0.75%.

E. Calculating the differential cross section

Data runs of like beam energy and scattering angle were combined into single kinematic points by summing the number of electrons in the event histograms and averaging the kinematic quantities. Since the position of the elastic peak is well defined at $W^2 = M_p^2 = 0.88$ (GeV)^2, both the event histogram $N(\Delta P, \Delta\Theta)$ and the acceptance function $F_{\rm acc}(\Delta P, \Delta\Theta)$ were converted to functions of the single variable W^2 using the relation

$$W^2 = M_p^2 + 2M_p\nu - Q^2. \tag{21}$$

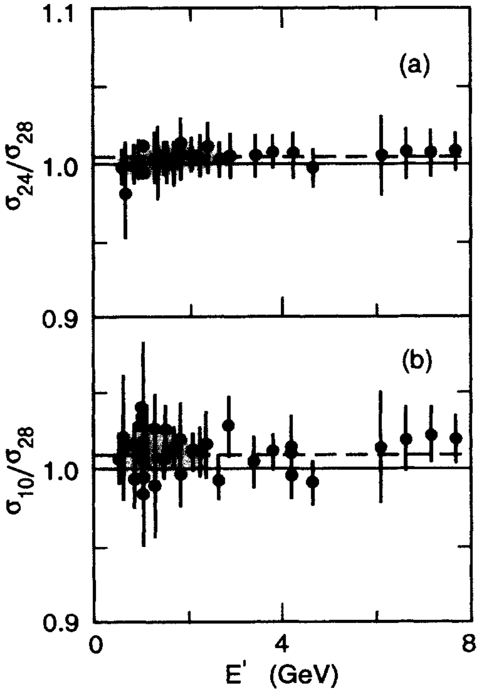

FIG. 19. $\Delta\Phi$ dependence of the 8 GeV acceptance. Plot (a) shows the ratio of 8 GeV cross sections obtained for restricted $\Delta\Phi$ cuts of ±24 mr to those obtained using the full ±28 mr cut plotted versus E'. Plot (b) illustrates similar ratios of cross sections obtained with the tightest cut of ±10 mr to ±28 mr. The results agree to better than 1% on average, shown by the dashed line, supporting that the $\Delta\Phi$ acceptance is well understood.

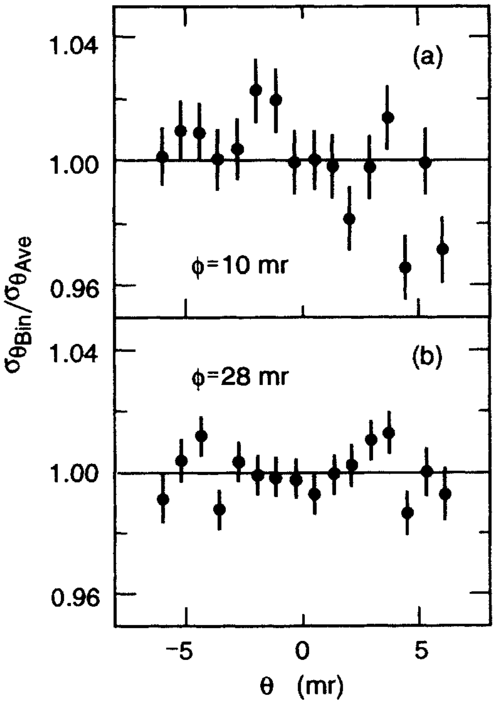

FIG. 20. $\Delta\Theta$ dependence of the 8 GeV acceptance. The ratio of 8 GeV cross sections obtained per $\Delta\Theta$ bin to those obtained for the full $\Delta\Theta$ range are plotted for two $\Delta\Phi$ cuts of 10 mr (a) and 28 mr (b). Since the θ dependence to the cross section has been previously divided out, the plots are expected to be flat. Within the errors the data support this indicating that the $\Delta\Theta$ dependence of the acceptance function was correctly modeled.

The differential cross section was then calculated in terms of measured quantities and correction factors as follows:

$$\frac{d\sigma}{d\Omega} = \frac{1}{Q_{\rm eff}}\,\frac{1}{n}\,\frac{X_{{\rm res}_{\rm corr}}}{R_{\rm corr}} \int^{W^2_{\rm cutoff}} \frac{N(W^2)}{F_{\rm acc}(W^2)}\,dW^2, \tag{22}$$

where the number of scattered electrons has been corrected for pion and aluminum end-cap backgrounds, and the acceptance function is in units of [sr (GeV)^2]. The integral over W^2 gives the total number of electrons detected within the spectrometer acceptance up to an arbitrary cutoff value, $W^2_{\rm cutoff}$, which will be discussed below. The factor $X_{{\rm res}_{\rm corr}}$ corrects for the number of events expected to lie above $W^2_{\rm cutoff}$ due to finite resolution effects, and was generally very close to unity.

The quantity $n = \rho_{\rm nom}\ell N_A/A$ gives the number of target nucleons per cm^2, where $\rho_{\rm nom}$ is the nominal hydrogen target density of 0.0707 g/cm^3, ℓ is the target length in cm, $N_A = 6.022 \times 10^{23}$ is Avogadro's number, and $A = 1.007$ g/mole is the atomic mass of the hydrogen. The variable $Q_{\rm eff}$ represents the effective incident charge per kinematic point. It is the product of several correction factors times the charge of the incident beam, summed over all runs at a given kinematic setting. Specifically,

$$Q_{\text{eff}} = \sum_{i=1}^{\text{No. of runs}} \frac{Q_i \; (E_{\text{corr}})_i}{(D_{\text{corr}})_i \; (\rho_{\text{corr}})_i}, \tag{23}$$

where Q_i is the number of incident electrons per run, E_{corr} is the efficiency of the detectors, D_{corr} is a correction for electronic and computer dead time, and $\rho_{\text{corr}} = \rho_{\text{nom}}/\rho$ is a correction to the nominal target density due to changes in incident beam current. By including the charge with the product of correction factors, one obtains the proper weighting of the cross section per incident beam charge when summing over several runs of a kinematic point.

1. *Integrating the elastic peak*

Figure 21 shows a typical elastic peak for the full range of W^2 with the arrow indicating the maximum upper limit for integration over W^2. Since this spectrum has not yet been corrected for higher radiative processes, the radiative tail is clearly visible at $W^2 > 0.9$ (GeV/c)^2. The lower limit of integration was chosen to be small enough to comfortably contain the peak, yet large enough to reduce the sensitivity to background events in the superelastic region. More important was the upper W^2 limit which was set large enough to include as much of the elastic peak as possible, yet small enough to avoid contributions from processes such as pion production which has a threshold at $W^2 = (m_e + m_\pi)^2 \sim 1.16$ GeV^2. To monitor sensitivity to this high W^2 cut, we calculated the cross sections for three different upper limits. No variation in the cross sections was observed within the statistical uncertainty of ±1%.

2. *Conversion to nominal kinematics*

Data at kinematic points were measured with similar, but not identical values of Q^2. To get all cross sections at the same Q^2 value so that Rosenbluth separations could be properly done, they were adjusted by the multiplicative factor

$$C_{\text{nom}} = \frac{\sigma_{\text{nom}}}{\sigma_{kp}}, \tag{24}$$

where σ_{kp} is a model cross section evaluated with the actual beam energy and spectrometer angle of the kinematic point, and σ_{nom} is a model cross section evaluated with the beam energy and angle of the nominal kinematics. The corrections were generally less than 1%, and thus insensitive to the choice of model.

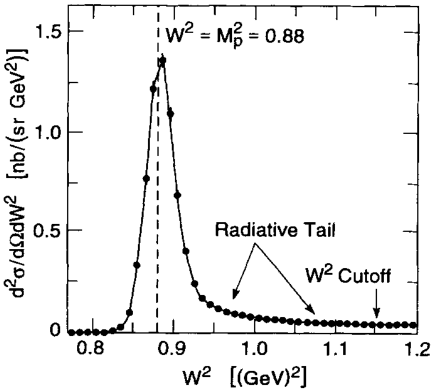

FIG. 21. A typical spectrum of the raw cross section plotted versus missing mass squared, W^2. The tail at high W^2 is due to higher-order radiative processes. The cross section was integrated up to the value specified by W^2_{cutoff} which was constrained to be less than 1.15 (GeV)^2 as indicated by the arrow.

Final values for the differential cross sections in (nb/sr) are given in Table IV corresponding to the nominal kinematics of each point.

IV. RESULTS AND COMPARISONS

A. Reduced cross sections

The measured differential cross sections were converted to reduced cross sections and divided by the square of the dipole form $G_D^2(Q^2)$ as follows:

$$\frac{\sigma_R}{G_D^2(Q^2)} \equiv \left(\frac{d\sigma}{d\Omega}\right) \frac{(1+\tau)}{5.18} \frac{\epsilon}{\tau} \frac{E^3}{E'} \frac{\sin^4(\frac{\theta}{2})}{\cos^2(\frac{\theta}{2})} \left(1 + \frac{Q^2}{0.71}\right)^4, \tag{25}$$

where the expression for the nonstructure cross section has been explicitly included, $(d\sigma/d\Omega)$ is the measured cross section in nb/sr, and all energies are in GeV. In a previous SLAC experiment, E136 [10], forward-angle cross sections were measured at $Q^2 = 8.83$ (GeV/c)^2. By combining these results with our 1.6 GeV 90° data at the same Q^2, we were able to effect a Rosenbluth separation at the highest Q^2 probed by this experiment.

The 1.6 GeV reduced cross sections were normalized to the 8 GeV results by fitting the 8 GeV reduced cross sections versus the virtual photon polarization, ϵ, at each of the five lowest Q^2 values where a minimum of at least two 8 GeV data points existed such that a linear fit could be performed. The normalization factor was that needed at each Q^2 to place the 1.6 GeV reduced cross section on the fitted line. The five resulting normalization factors were found to be independent of Q^2, as expected, and the factor 0.958 ±0.007, obtained for the lowest Q^2 point, was applied for all Q^2 points. The deviation of the normalization from unity by roughly 4% has been attributed to the uncertainty in the magnitude of the 1.6 GeV acceptance function. Because of the normalization, the 1.6 GeV reduced cross sections were assigned an additional point-to-point systematic error of ±0.7%.

B. Errors in the reduced cross section

The point-to-point systematic errors in the reduced cross sections were determined by taking the quadrature sum of the point-to-point uncertainties in all quantities which define the cross section: the incident charge (0.2%), target density (0.2%), detector efficiency (0.2%

and 0.3% for the 8 GeV and 1.6 GeV detectors, respectively), electronic and computer dead time (0.2%), beam energy (0.06%), scattering angle (0.006° and 0.05° for the 8 GeV and 1.6 GeV angles, respectively), background pion subtraction (negligible), aluminum end-cap subtraction (0.2%), radiative corrections (0.5%), spectrometer acceptance (0.5% and 0.75% for the 8 GeV and 1.6 GeV acceptances, respectively), and in the case of the 1.6 GeV data, an error due to the normalization (0.7%). The quadrature sum of the resulting uncertainties produced in the reduced cross sections due to the above errors was 1.06% for the 8 GeV data and 1.32% for the 1.6 GeV data. The total point-to-point uncertainty in reduced cross sections was given by the quadrature sum of the statistical error ($\simeq$ 1%) and the point-to-point systematic error.

In addition to the point-to-point errors, an overall normalization uncertainty of 1.77% was applied to all cross sections based on the quadrature sum of the systematic uncertainties in incident charge (0.5%), target density (0.9%), beam energy (0.05%), radiative corrections (1.0%), and the 8 GeV acceptance function (1.0%).

C. Elastic form factor results

The reduced cross sections divided by the square of the dipole fit were plotted versus ϵ at each Q^2 as shown in Fig. 22, and fit with a straight line yielding a slope and intercept given by $G_{E_p}^2/\tau G_D^2$ and $G_{M_p}^2/G_D^2$, respectively. The average χ^2 per degree of freedom was 1.11. The Dirac and Pauli form factors $F_1(Q^2)$ and $F_2(Q^2)$ were also determined by $F_1(Q^2) = [\tau G_M(Q^2) + G_E(Q^2)]/(1+\tau)$ and $F_2(Q^2) = [G_M(Q^2) - G_E(Q^2)]/\kappa_p(1+\tau)$.

The reported form factor values and their corresponding statistical errors result from a fit to the reduced cross sections weighted *only* by their statistical errors. The total point-to-point errors on the form factors were determined by fitting the data a second time weighted by the

TABLE IV. Measured cross sections. The measured elastic cross sections are given in units of nb/sr. The total point-to-point error is obtained by adding the statistical and the systematic point-to-point errors in quadrature. In addition to the total point-to-point error, there is an overall normalization uncertainty of ±1.77% which has not been included in the errors listed in the table.

Q^2 (GeV/c)^2	E (GeV)	Θ (degrees)	E' (GeV)	ϵ	$\frac{d\sigma}{d\Omega}$ (nb/sr)	± Stat. error	± Total error
			8 GeV cross sections				
1.75	1.511	90.066	0.578	0.250	1.440×10^{-1}	1.116×10^{-3}	1.750×10^{-3}
1.75	2.407	41.110	1.474	0.704	1.029×10^{0}	4.715×10^{-3}	1.090×10^{-2}
1.75	5.507	15.145	4.574	0.950	$1.155\times10^{+1}$	6.713×10^{-2}	1.336×10^{-1}
2.50	1.968	89.947	0.636	0.227	3.389×10^{-2}	3.616×10^{-4}	4.832×10^{-4}
2.50	2.407	58.882	1.075	0.47	9.857×10^{-2}	9.199×10^{-4}	1.317×10^{-3}
2.50	2.837	44.993	1.505	0.630	1.990×10^{-1}	1.811×10^{-3}	2.638×10^{-3}
2.50	3.400	34.694	2.068	0.750	3.951×10^{-1}	1.849×10^{-3}	4.266×10^{-3}
2.50	3.95	28.409	2.624	0.820	6.616×10^{-1}	4.025×10^{-3}	7.637×10^{-3}
2.50	5.507	18.981	4.175	0.913	1.779×10^{0}	1.147×10^{-2}	2.120×10^{-2}
3.25	2.837	61.205	1.105	0.426	2.848×10^{-2}	3.499×10^{-4}	4.444×10^{-4}
3.25	3.400	44.482	1.668	0.609	6.784×10^{-2}	5.949×10^{-4}	8.885×10^{-4}
3.25	3.956	35.382	2.224	0.719	1.256×10^{-1}	1.075×10^{-3}	1.636×10^{-3}
3.25	5.507	22.804	3.775	0.865	3.898×10^{-1}	1.888×10^{-3}	4.343×10^{-3}
4.00	3.400	57.572	1.268	0.437	1.297×10^{-2}	1.858×10^{-4}	2.243×10^{-4}
4.00	3.956	43.707	1.824	0.593	2.770×10^{-2}	3.474×10^{-4}	4.407×10^{-4}
4.00	4.507	35.592	2.375	0.694	4.929×10^{-2}	6.162×10^{-4}	7.853×10^{-4}
4.00	5.507	26.823	3.375	0.805	1.023×10^{-1}	9.097×10^{-4}	1.370×10^{-3}
4.00	9.800	13.248	7.668	0.946	6.180×10^{-1}	4.679×10^{-3}	8.073×10^{-3}
5.00	3.956	59.291	1.291	0.389	4.205×10^{-3}	8.647×10^{-5}	9.565×10^{-5}
5.00	4.507	45.658	1.842	0.538	8.462×10^{-3}	1.239×10^{-4}	1.492×10^{-4}
5.00	5.507	32.829	2.842	0.704	2.128×10^{-2}	2.228×10^{-4}	3.079×10^{-4}
5.00	9.800	15.367	7.135	0.919	1.576×10^{-1}	1.643×10^{-3}	2.338×10^{-3}
6.00	9.800	17.515	6.603	0.886	4.749×10^{-2}	5.879×10^{-4}	7.705×10^{-4}
7.00	9.800	19.753	6.070	0.847	1.707×10^{-2}	3.860×10^{-4}	4.249×10^{-4}
			1.6 GeV cross sections				
1.75	1.511	90.066	0.578	0.250	1.514×10^{-1}	3.132×10^{-4}	1.690×10^{-3}
2.50	1.968	89.947	0.636	0.227	3.545×10^{-2}	1.008×10^{-4}	4.044×10^{-4}
3.25	2.407	90.004	0.675	0.206	1.095×10^{-2}	7.314×10^{-5}	1.418×10^{-4}
4.00	2.837	89.966	0.705	0.190	4.092×10^{-3}	3.323×10^{-5}	5.636×10^{-5}
5.00	3.40	89.985	0.735	0.171	1.339×10^{-3}	1.242×10^{-5}	1.942×10^{-5}
6.00	3.956	89.981	0.759	0.156	5.164×10^{-4}	6.577×10^{-6}	8.747×10^{-6}
7.00	4.507	89.991	0.777	0.143	2.248×10^{-4}	5.088×10^{-6}	5.675×10^{-6}
8.83	5.507	90.016	0.784	0.125	6.022×10^{-5}	2.344×10^{-6}	2.439×10^{-6}

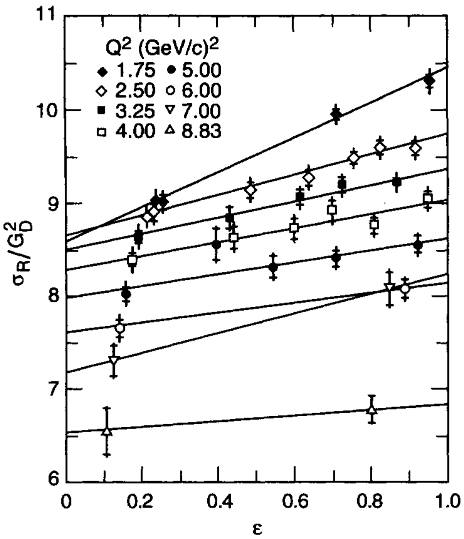

FIG. 22. Reduced cross sections divided by the square of the dipole fit plotted versus ϵ for each value of Q^2. The 1.6 GeV data points correspond to the leftmost point on each line, and the E136 data point is the rightmost point on the $Q^2 = 8.83$ (GeV/c)^2 line. The inner error bars show the statistical error, while the outer error bars show the total point-to-point uncertainty, given by the quadrature sum of the statistical and point-to-point systematic errors. An overall normalization uncertainty of ±1.77% has not been included.

total point-to-point errors. For each fit, care was taken to account for correlations between the variables by adjusting the fitted parameters until the χ^2 value increased by one. This technique was applied twice, once increasing the slope and once decreasing the slope, to map out the χ^2 contour. The difference between the augmented and original values of the slope and intercept were added and subtracted to the original fitted parameters yielding the upper and lower error bars, respectively.

The results for the elastic form factors divided by the dipole fit are shown in Figs. 23 and 24 and listed in Tables V and VI. The inner error bars correspond to the statistical error while the outer bar gives the total point-to-point uncertainty. An additional overall normalization uncertainty of ±0.9% in the form factors alone has not been included. In the region of overlap with data from previous experiments [3–7], the new results are in general agreement and have significantly smaller errors. Our results for G_{E_p} are consistent with the dipole fit within the 5–20% errors as shown in Fig. 23, while G_{M_p} rises above the dipole fit by 5% at $Q^2 = 2$ (GeV/c)^2 and falls below it by 8% $Q^2 = 9$ (GeV/c)^2 as shown in Fig. 24, deviations significant compared with the $\simeq 1\%$ errors.

To the extent that the charge and magnetic moment distributions have the same spatial dependence, form factor scaling is expected to hold: namely,

$$G_{E_p}(Q^2) = G_{M_p}(Q^2)/\mu_p. \tag{26}$$

However, Fig. 25 indicates that form factor scaling is only approximate since deviations of 20% are observed in the range $Q^2 = 1 - 3$ (GeV/c)^2.

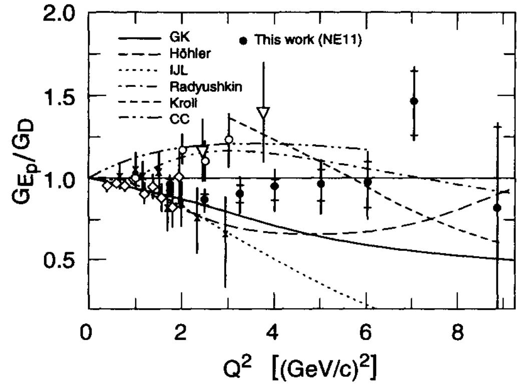

FIG. 23. Extracted values for G_{E_p}/G_D compared with previous data and several models and predictions. The crosses are from Bartel *et al.* Ref. [3], the diamonds from Berger *et al.* Ref. [4], the inverted triangles from Litt *et al.* Ref. [5], and the open circles from Walker *et al.* Ref. [6]. The solid line (GK) is from Ref. [35], the long dashed line (Höhler) is from Ref. [31], the dotted line (IJL) is from Ref. [32], the dashed-dot line (Radyushkin) is from Ref. [37], the short dashed line (Kroll) is from Ref. [40], and the dashed double-dot line (CC) is from Ref. [38].

D. Comparison with theory

Although the dipole form approximates the Q^2 dependence of the data, the physical insight it provides is limited. Many approaches have been undertaken to try and understand the form factors. Some of the most common of these are discussed below.

1. Vector meson dominance models

Vector meson dominance (VMD) models describe the photon-nucleon interaction via the intermediary coupling with vector mesons. The Feynman diagram for the process is shown in Fig. 26. The nucleon form factors, can then be written as a sum over meson propagators times

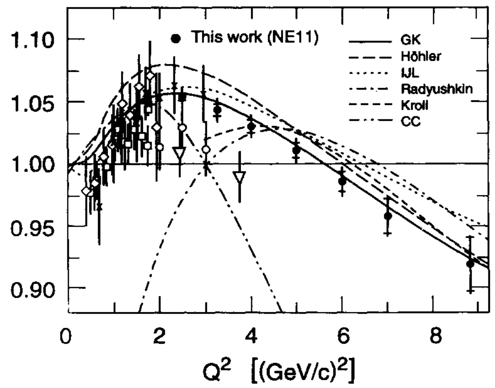

FIG. 24. Extracted values for $G_{Mp}/\mu_p G_D$. The squares are from Bosted *et al.* Ref. [7], otherwise all previous data and model curves are as noted in Fig. 23.

TABLE V. The extracted values for the electric and magnetic form factors scaled by the dipole fit are presented. The ratio of electric and magnetic form factors is also given. The total error is the quadrature sum of the statistical plus the systematic point-to-point error. An overall normalization error of ±0.9% in the form factors has not been included.

Q^2 $(\mathrm{GeV}/c)^2$	$\frac{G_{E_p}}{G_D}$	Stat. error	Total error	$\frac{G_{M_p}}{\mu_p G_D}$	Stat. error	Total error	$\frac{\mu_p G_{E_p}}{G_{M_p}}$	Stat. error	Total error
1.75	0.956	+0.032 −0.033	+0.053 −0.056	1.050	+0.006 −0.006	+0.010 −0.010	0.910	+0.036 −0.036	+0.059 −0.061
2.50	0.868	+0.023 −0.024	+0.065 −0.070	1.054	+0.002 −0.002	+0.007 −0.007	0.824	+0.024 −0.024	+0.068 −0.072
3.25	0.884	+0.051 −0.055	+0.108 −0.123	1.045	+0.005 −0.005	+0.009 −0.009	0.846	+0.053 −0.056	+0.112 −0.124
4.00	0.919	+0.066 −0.071	+0.118 −0.135	1.031	+0.005 −0.005	+0.009 −0.009	0.891	+0.068 −0.073	+0.123 −0.138
5.00	0.942	+0.094 −0.104	+0.155 −0.188	1.012	+0.006 −0.006	+0.009 −0.009	0.931	+0.099 −0.108	+0.162 −0.192
6.00	0.952	+0.133 −0.155	+0.184 −0.229	0.987	+0.008 −0.008	+0.012 −0.012	0.965	+0.144 −0.164	+0.200 −0.241
7.00	1.448	+0.184 −0.211	+0.209 −0.244	0.959	+0.014 −0.014	+0.016 −0.016	1.510	+0.217 −0.238	+0.247 −0.275
8.83	0.869	+0.464 −0.869	+0.484 −0.869	0.916	+0.022 −0.022	+0.023 −0.023	0.948	+0.542 −0.948	+0.566 −0.948

TABLE VI. The extracted values for the Dirac and Pauli form factors scaled by the dipole form are given. The ratio of $Q^2 F_2/F_1$ is also given. The errors are defined as in Table V.

Q^2 $(\mathrm{GeV}/c)^2$	$\frac{F_1}{G_D}$	Stat. error	Total error	$\frac{F_2}{G_D}$	Stat. error	Total error	$\frac{Q^2 F_2}{F_1}$	Stat. error	Total error
1.75	1.613	+0.016 −0.017	+0.026 −0.028	0.737	+0.018 −0.018	+0.031 −0.030	0.799	+0.029 −0.027	+0.048 −0.044
2.50	1.731	+0.011 −0.011	+0.030 −0.033	0.677	+0.010 −0.010	+0.029 −0.028	0.978	+0.021 −0.020	+0.062 −0.056
3.25	1.860	+0.021 −0.022	+0.043 −0.051	0.590	+0.019 −0.019	+0.043 −0.039	1.031	+0.047 −0.043	+0.106 −0.089
4.00	1.962	+0.023 −0.025	+0.041 −0.050	0.512	+0.022 −0.021	+0.042 −0.037	1.044	+0.060 −0.054	+0.115 −0.097
5.00	2.047	+0.029 −0.034	+0.049 −0.062	0.434	+0.028 −0.025	+0.049 −0.042	1.060	+0.087 −0.076	+0.160 −0.126
6.00	2.089	+0.035 −0.043	+0.047 −0.064	0.372	+0.037 −0.032	+0.054 −0.045	1.069	+0.130 −0.108	+0.194 −0.149
7.00	2.266	+0.036 −0.044	+0.040 −0.052	0.230	+0.047 −0.042	+0.054 −0.047	0.709	+0.161 −0.137	+0.187 −0.156
8.83	2.077	+0.088 −0.205	+0.091 −0.202	0.269	+0.148 −0.084	+0.148 −0.087	1.143	+0.821 −0.387	+0.821 −0.403

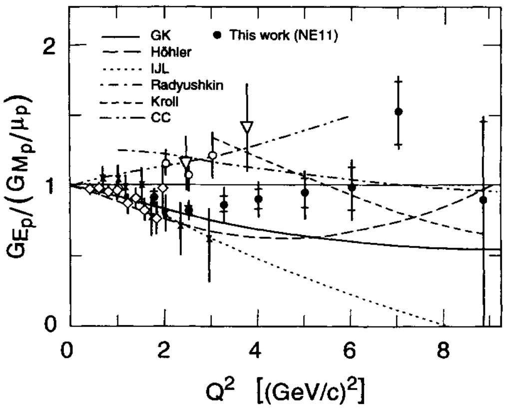

FIG. 25. Results for $G_{E_p}/(G_{M_p}/\mu_p)$ indicate form factor scaling is only approximate. Previous data and model curves are as noted in Fig. 23.

the meson nucleon form factor:

$$F(Q^2) = \sum_i \frac{C_{\gamma V_i}}{Q^2 + M_{V_i}^2} F_{V_i N}(Q^2), \tag{27}$$

where $1/(Q^2 + M_{V_i}^2)$ is the propagator associated with a meson of mass M_{V_i}, $C_{\gamma V_i}$ is the photon-meson coupling strength, and $F_{V_i N}$ is the meson-nucleon form factor.

VMD models differ according to their inclusion of different meson states. All models include the lowest mass mesons ρ and ω, while only some incorporate those of higher mass such as the ω', ρ'' and the strange meson, ϕ. Some models take into account the meson width, others do not. However, all models share the common plight that they are not fundamental theories since they do not predict the number or masses of the mesons, and their success is generally limited to the lower Q^2 domain.

The fits of Höhler *et al.* [31] use effective pole terms for the ρ' ($\sim$ 1.25 GeV), ω' ($\sim$ 1.25 GeV), and ϕ ($\sim$ 1 GeV) exchanges, but treat the ρ exchange more completely using pion-nucleon amplitudes and the pion form factor as inputs. In Figs. 23 and 24 we compare the present data with Höhler Fit 5.3, which gave the best agreement with previous data. The model shows a dip for $G_{E_p}(Q^2)$ between $Q^2 = 2 - 8$ (GeV/c)^2, which underestimates the data by as much as 20%, and a rise above the dipole fit as Q^2 increases beyond 8 (GeV/c)^2. Although the data do not support a dip as large as that of the model, a slight dip in the same Q^2 region cannot be ruled out. For G_{M_p}, the model gives the correct asymptotic Q^2 dependence to the data but overestimates the magnitude of the bump in the region $Q^2 = 1 - 4$ (GeV/c)^2. It should be noted that Fit 8.2, which includes more effective poles and is fit to both proton and neutron data, gives good agreement with our results for G_{E_p}, however, further overestimates G_{M_p}.

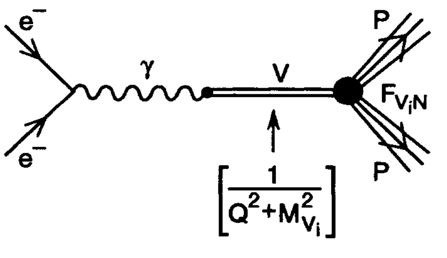

FIG. 26. Feynman diagram for vector meson dominance models.

Another commonly used VMD fit is that of Iachello, Jackson, and Lande [32] (IJL), which includes couplings for the ρ, ω, and ϕ mesons as parameters, as well as the width of the ρ meson. For G_{E_p} this model is in poor agreement with our results over the entire Q^2 range, having too rapid a fall-off with increasing Q^2. For G_{M_p}, the model does slightly better in that it characterizes the bump observed for $Q^2 = 1 - 4$ (GeV/c)^2 and then approaches the predicted asymptotic fall-off of Q^{-4}, although not quite rapidly enough.

Although neither model presented here is able to fully characterize the Q^2 dependence of the new data, new fits incorporating the present data should be done before conclusions about the limitations of the VMD approach can be drawn.

2. Dimensional scaling

Dimensional counting rules [33] state that by counting the number of elementary particles or fields present in the initial and final states of an exclusive interaction, one can determine the asymptotic Q^2 dependence of the reaction. The mechanism responsible for this result comes from the hard rescattering of the pointlike quarks, and this result has been validated within the confines of PQCD, modulo the logarithmic terms. Dimensional counting gives the following Q^2 dependence of the cross section in the limit $Q^2 \to \infty$:

$$\frac{d\sigma}{dQ^2}(AB \to CD) \sim [Q^2]^{2-n}, \tag{28}$$

where n is the sum number of elementary particles participating in the interaction. For electron proton scattering $n = 8$ due to three quarks and one electron in both the initial and final states. In the limit of large Q^2, the cross section in the single photon approximation is dominated by F_1:

$$\frac{d\sigma}{dQ^2} \propto \frac{1}{Q^4} F_1^2(Q^2). \tag{29}$$

Using these relations, we find, for large Q^2, $F_1 \propto Q^{-4}$. For the helicity-nonconserving term F_2, dimensional scaling predicts an additional factor of Q^{-2} due to the extra quark helicity-flip associated with the helicity nonconserving part of the scattering amplitude, thereby giving $F_2 \propto Q^{-6}$.

If dimensional scaling laws are correct, the ratio Q^2F_2/F_1 is expected to approach a constant at sufficiently large Q^2. Comparison with our data in Fig. 27 indicates that the ratio is flattening out at $Q^2 = 3 - 4$ (GeV/c)^2.

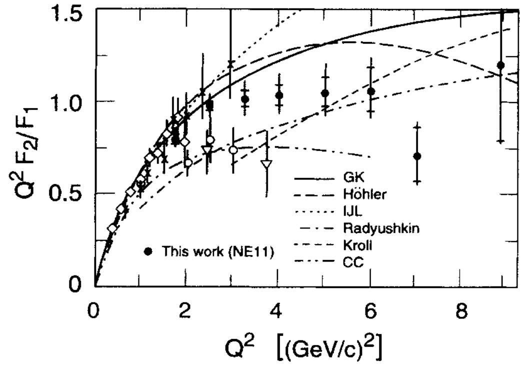

FIG. 27. Results for the ratio Q^2F_2/F_1. Previous data and model curves are the same as noted in Fig. 23.

3. *Hybrid models*

There have been several attempts to reconcile the success of the VMD models at low Q^2 with the asymptotic Q^2 dependence predicted by PQCD. These hybrid models [34,35] are constrained to give the monopole form of meson physics in the low Q^2 region and to exhibit the characteristic Q^2 fall-off dictated by PQCD for the high Q^2 region. The parameters for the coupling strengths, scale factors, and masses are extracted from fits to existing form factor data. Because of their constraints at both low and high Q^2, these phenomenological models tend to achieve reasonable agreement with the data in the moderate Q^2 region.

One model which will be presented here, that of Gari and Krümpelmann [35], incorporates only the ρ and ω mesons. The electromagnetic form factors are written as a product of the usual vector meson pole terms and a meson-nucleon form factor F_{VN}, assumed to be the same for all vector mesons, i.e., $F_{VN_\rho} = F_{VN_\omega} = F_{VN}$. The form for the meson-nucleon form factors is chosen so that at low Q^2 they behave as dictated by meson physics and thus reduce to a monopole, and at high Q^2 they illustrate the asymptotic Q^{-4} and Q^{-6} fall-off as predicted by PQCD.

Comparison with our data indicates that G_{M_p} is very well described by the model. The electric form factor, however, is well described for $Q^2 \leq 3$ (GeV/c)^2, but above that, the model has too strong a Q^2 fall-off. As noted by the authors, since G_{E_p} is determined by the difference of two large numbers, F_1 and F_2, slight changes in the coupling strengths can have big effects. Thus, refitting the model with this new data will likely give better agreement for the electric form factor.

4. *QCD sum rules*

The accurate description of the nucleon form factors at low Q^2 requires nonperturbative techniques [1]. One such technique, the QCD sum rule [36] approach, is based on the concept of quark-hadron duality, namely, that characteristics of the hadronic spectrum are similar to analogous characteristics for free quarks as computed in perturbation theory. A model developed by Radyushkin [37] uses QCD sum rules to fix the parameters of the soft wave function of the proton. The model makes predictions for both neutron and proton form factors in the moderate Q^2 region which, Radyushkin argues, are dominated by the lowest-order nonperturbative diagrams, i.e., no hard gluon exchange.

The structure for factorization of the nucleon form factors in terms of the long- and short-range contributions is given in Fig. 28, where the short-range contributions, due to hard gluon exchanges, are indicated by the dashed lines. Radyushkin argues that for low Q^2, only the long-range contributions are important since higher-order diagrams get suppressed by a factor $\alpha_s(M_N)/\pi$ for each gluon exchange.

Figure 23 shows that although the predicted electric form factor lies above the data for $Q^2 \leq 5$ (GeV/c)^2, better agreement is obtained for $Q^2 > 5$ (GeV/c)^2. The model is not expected to work well for $Q^2 < 3$ (GeV/c)^2, and as indicated in Fig. 24, it does not, falling well below the data. Yet, for $Q^2 \geq 4$ (GeV/c)^2 it gives reasonable agreement with experimental results for G_{M_p}, correctly describing the Q^2 dependence, but overestimating the magnitude by a few percent.

5. *Constituent quark model*

Constituent quark models [38,39] represent mesons and baryons as bound states of two and three quarks such that all degrees of freedom are embodied by properties of the quarks. The quarks are nonpointlike, and hence have form factors associated with them which are Q^2 dependent. In the simplified model of Chung and Coester [38], the constituent quarks are considered to be sufficiently small that this Q^2 dependence can be neglected. This limits the applicability of this model to $Q^2 \leq 6$ (GeV/c)^2, above which the Q^2 dependence of the quark form factors must be taken into account.

The model expresses the isoscalar and isovector nucleon form factors in terms of nucleon current matrix elements which are calculated using a quark-model wave

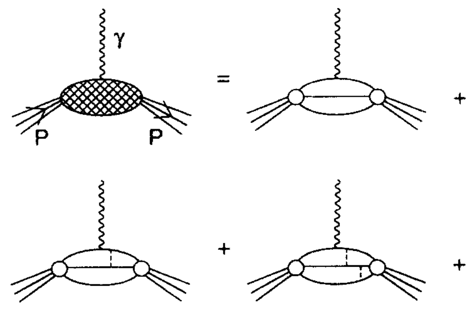

FIG. 28. The QCD diagrams showing the factorization of the photon-hadron vertex in terms of long- and short-range contributions. The lowest-order diagrams do not contain short-range contributions (indicated by dashed lines) due to hard gluon exchange between the quarks.

function for the nucleon. The wave function is symmetric in the quark variables of null-plane momenta, spin, and isospin and depends on only two parameters: a quark confinement scale $1/\alpha$ and the quark mass m_q. The model was used to calculate the nucleon form factors for several combinations of m_q and α for $Q^2 = 0 - 6$ $(\mathrm{GeV}/c)^2$. Reasonable agreement with the available data was found for a quark mass less than the somewhat conventional nonrelativistic choice of one third the nucleon mass. The values $m_q = 0.24$ GeV and $\alpha = 0.635$ GeV provide the best agreement [38] with the data from Ref. [6]. For $Q^2 \leq 2$ $(\mathrm{GeV}/c)^2$ the model gives reasonable agreement for G_{M_p}, but then falls off rapidly, while the model lies above the data for G_{E_p}. Other values for the quark mass may give better agreement with the new data.

6. Diquark model

Quark degrees of freedom are also included in those models which simplify the three-body physics of the nucleon by considering two tightly bound quarks as a single constituent called a diquark (D). Diquark models, like constituent quark models, introduce Q^2-dependent form factors to account for the finite size of the diquarks, and use a nucleon wave function or distribution amplitude (DA) which contains quark degrees of freedom.

The model presented here from Kroll *et al.* [40] specifically addresses the moderate Q^2 region, but is constrained to agree with the pure quark model [41] in the asymptotic region. In analogy to the hard scattering picture by Lepage and Brodsky [42], the photon-nucleon vertex is expressed by a convolution of DA's with amplitudes for elementary subprocesses between the internal constituents calculated in a collinear approximation within PQCD. The model uses two different DA's both obtained from the harmonic oscillator wave function transformed to the light cone.

The $\gamma N \rightarrow N$ vertex contains the sum over all elementary subprocesses of the form $\gamma q D \rightarrow q D$. In an attempt to incorporate quark helicity flips, the model includes spin 1 and spin 0 diquarks. These give rise to the four subprocess diagrams illustrated in Fig. 29. The blobs correspond to three- and four-point functions describing the couplings of the photons and gluons to the diquarks. The amplitudes of the four diagrams are obtained by first calculating the three- and four-point functions for point-like quarks, and then multiplying them by diquark form factors which are parametrized to give the correct asymptotic results of Lepage and Brodsky.

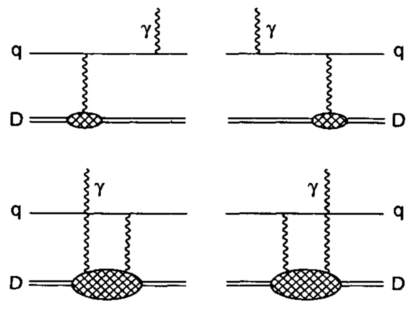

FIG. 29. The four subprocess diagrams of the form $\gamma q D \rightarrow q D$ used in the diquark model. The blobs correspond to the three- and four-point functions which incorporate the photon and gluon couplings to the diquark (D). Since both spin 0 and spin 1 diquarks are considered, there are four diagrams.

The model using DA 2.13 was first fit to previous data [10] for G_{M_p} for $Q^2 = 3.3 - 33$ GeV/c^2, and then the parameters were fine-tuned by performing a common fit to both G_{M_p} and Compton scattering data. Comparison with the new data indicates that the model gives a fairly good description of G_{M_p} but does poorly when compared with $G_{E_p}(Q^2)$.

V. CONCLUSIONS

Elastic ep cross sections were measured with an average total uncertainty of $< 2.0\%$ for energies from 1.5 to 9.8 GeV and for an angular range $13.2^\circ \leq \theta \leq 90^\circ$. The proton elastic form factors $G_{E_p}(Q^2)$ and $G_{M_p}(Q^2)$ were extracted from Rosenbluth separations performed at eight Q^2 values: 1.75, 2.50, 3.25, 4.00, 5.00, 6.00, 7.00, and 8.83 $(\mathrm{GeV}/c)^2$, more than doubling the range of existing data. In the region of overlap for $Q^2 < 4$ $(\mathrm{GeV}/c)^2$, the new results are in satisfactory agreement with previous data, and the total errors have been considerably reduced to $< 14\%$ in G_{E_p} and $< 1.5\%$ in G_{M_p}.

The electric form factor is best described by a dipole dependence, while the magnetic form factor scaled by the dipole form falls smoothly from 1.05 to 0.92 and is best described by the hybrid model of Gari and Krümpelmann [35]. Deviations from form factor scaling, $G_{E_p} = G_{M_p}/\mu_p$, are observed up to 20% in the region $Q^2 = 2$ $(\mathrm{GeV}/c)^2$. Thus, form factor scaling only approximates the Q^2 dependence of the form factors. The ratio of Pauli and Dirac form factors $Q^2 F_2/F_1$ approaches a constant for $Q^2 \geq 3$ $(\mathrm{GeV}/c)^2$.

Comparisons made with VMD parametrizations, dimensional scaling, diquark, and constituent quark models indicate that none of the above are able to characterize both form factors over the entire Q^2 range. Since many of the models rely on fits to previous data, refitting those models with the current data will most likely yield better agreement.

ACKNOWLEDGMENTS

We acknowledge the support of the SLAC management and staff, especially G. Davis, R. Eisele, C. Hudspeth, and J. Mark. This work was supported in part by National Science Foundation Grants Nos. PHY-87-15050 (AU), PHY-89-18491 (Maryland), PHY-88-19259 (U Penn), and PHY-86-58127 (UW), by Department of Energy Contracts Nos. DE-AC03-76SF00515 (SLAC), W-7405-ENG-48 (LLNL), DE-FG02-88ER40415 (U Mass), DE-AC02-ER13065 (UR), and DE-FG06-90ER40537 (UW), and by the U.S.-Israel Binational Science Foundation.

APPENDIX: ELASTIC PEAK CALIBRATION

The kinematics of elastic scattering are constrained such that $W^2 = M_p^2 = 0.88035$ (GeV)^2. Invoking this constraint provides a useful means of calibrating the kinematics since any observed deviation from M_p^2 in the elastic peak, can be compensated by shifting one or more of the kinematic variables E, E', and θ. The shift necessary to center a given W^2 peak at M_p^2 can be calculated for each kinematic variable, assuming no shift in the other two, resulting in

$$\frac{dE}{E} = \frac{dW^2}{2M_pE'}, \quad \frac{dE'}{E'} = \frac{-dW^2}{2M_pE}, \quad d\theta = \frac{-dW^2}{2EE'\sin\theta}, \tag{A1}$$

where the constraint $2M_p(E - E') = 4EE'\sin^2(\frac{\theta}{2})$ has been applied, and $dW^2 = W^2_{\text{peak}} - M_p^2$.

To compare the W^2 peak positions, it is first necessary to correct radiatively the spectra. Recall that the raw W^2 spectra had a large tail at low E' due to radiative processes other than the single photon exchange. This tail causes the position of the peak to be shifted to higher W^2. To find the true position of the peak, a radiative corrections procedure [43,44] was used which corrected the counts in each W^2 bin for radiative losses. This process was referred to as "deradiating" the elastic peaks, and it was used to obtain the peak positions and widths for the purposes of calibrating the kinematic variables, determining the resolution function which was particular to each spectrometer, and verifying that the contribution to the cross section from superelastic events was consistent with zero. Figure 30 illustrates a typical W^2 spectra both before and after the deradiating process.

1. Deviations in kinematic variables

Fits to the deradiated peaks indicated that they were not centered at $W^2 = M_p^2$, but were shifted slightly to $W^2 < M_p^2$ for data from both spectrometers. (These results are consistent with those found by Walker [45] in a similar elastic peak calibration of 8 GeV data.) The 8 GeV data were used to cross-calibrate the beam energy since the central momentum and angle were precisely known. Results from fits to the 8 GeV peaks are shown in Fig. 31, where the offset in W^2 has been alternately translated into respective shifts in E', E, and θ needed to center the peaks. Each point corresponds to a kinematic setting, and the errors are given by the statistical error calculated from the number of counts in the peak added in quadrature with the statistical error in the quantity plotted on the abscissa. The dot-dashed line indicates the shift needed to center the peaks on average. This can be compared with the dotted line which shows the maximum shift allowed by the systematic error in the quantity.

The peaks can be centered by changing one or a combination of the three kinematic variables E, E', and θ. The criteria used in deciding which variables would be offset were (a) any offset would not exceed the uncertainty in that variable, and (b) a fit to the resultant peak positions would have a minimum χ^2. Centering the 8 GeV spectrometer peaks by shifting θ would require an average shift of 0.024°. However, this is four times greater than the uncertainty in the scattering angle determined from the survey data, and is unreasonable. The average shift needed to center the peaks by shifting E' was 0.04%, however this was larger than the uncertainty at high E'. Although the average shift needed to center the peaks by changing the beam energy was 0.09%, within the ±0.1% uncertainty of the flip coil measurement of incident beam energy, it was found that the best χ^2 was achieved by splitting the offset between E and E'. Thus

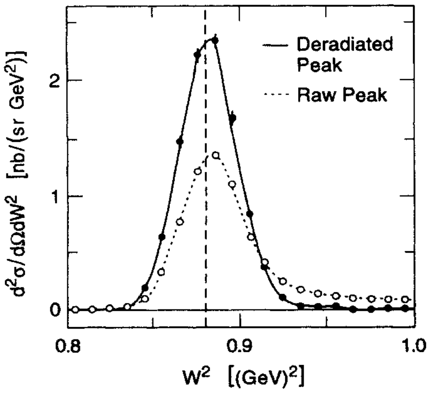

FIG. 30. A typical elastic peak spectrum shown before deradiating, the dotted curve, and after deradiating, the solid curve.

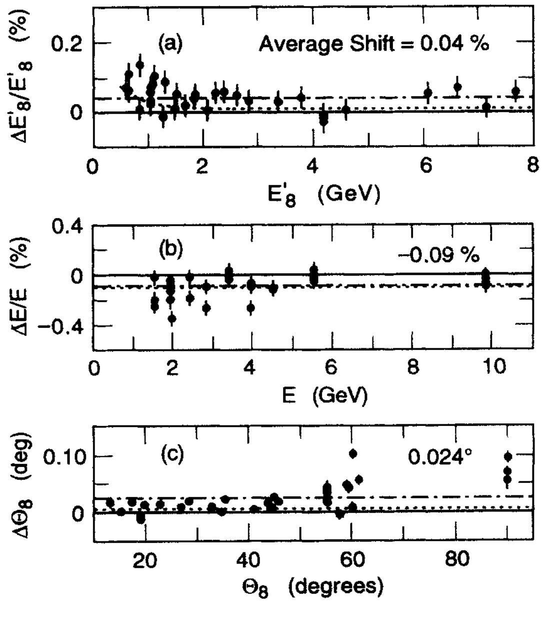

FIG. 31. Plots (a), (b), and (c) show the shifts in E', E, and θ, respectively, necessary to center the W^2 peak at M_p^2 for each kinematic point. The dot-dashed line in each plot corresponds to the shift needed to center the peaks on average. The dashed curve represents the maximum shift allowed by the systematic error in the respective variable.

E' was shifted according to its maximum systematic error which is a function of E', indicated by the dotted line in plot (a), and E was shifted by 0.04%, the amount necessary to completely center the peaks at M_p^2.

With the W^2 peaks centered on average, the residual scatter was used to estimate the point-to-point uncertainty in beam energy yielding a sigma of 0.06%. This was consistent with the energy slit settings, and amounted to a conservative estimate of the error since fluctuations in magnetic fields and the spectrometer angle also contribute to the observed spread in peak positions.

Performing a similar analysis for the 1.6 GeV elastic peaks indicated that the best χ^2 was obtained by shifting E' by 0.14% which was within the ±0.3% uncertainty in central momentum.

[1] V. L. Chernyak and A. R. Zhitnitsky, Phys. Rep. **112**, 173 (1984).
[2] Particle Data Group, K. Hikasa *et al.*, Phys. Rev. D **45**, S1 (1992), p. III.54. A list of relevant references can be found under the heading QCD.
[3] W. Bartel *et al.*, Nucl. Phys. **B58**, 429 (1973).
[4] Ch. Berger *et al.*, Phys. Lett. **35B**, 87 (1971).
[5] J. Litt *et al.*, Phys. Lett. **31B**, 40 (1970).
[6] R. C. Walker *et al.*, Phys. Lett. B **224**, 353 (1989); **240**, 522 (1990); Phys. Rev. D **49**, 5671 (1993).
[7] P. E. Bosted *et al.*, Phys. Rev. C **42**, 38 (1990); A. T. Katramatou *et al.*, Nucl. Instrum. Methods Phys. Res. Sect. A **267**, 448 (1988).
[8] R. G. Arnold *et al.*, Phys. Rev. Lett. **61**, 806 (1988).
[9] A. S. Esaulov *et al.*, Yad. Fiz. **45**, 410 (1987) [Sov. J. Nucl. Phys. **45**, 258 (1987)].
[10] R. Arnold *et al.*, Phys. Rev. Lett. **57**, 174 (1986); A. F. Sill *et al.*, Phys. Rev. D **48**, 29 (1993).
[11] S. Rock *et al.*, Phys. Rev. Lett. **49**, 1139 (1982).
[12] P. E. Bosted *et al.*, Phys. Rev. Lett. **68**, 3841 (1992).
[13] A. Lung *et al.*, Phys. Rev. Lett. **70**, 718 (1993).
[14] M. N. Rosenbluth, Phys. Rev. **79**, 615 (1950).
[15] L. Clogher, Ph.D. thesis, The American University, 1993.
[16] A. Lung, Ph.D. thesis, The American University, 1992.
[17] L. M. Stuart, Ph.D. thesis, University of California, Davis, 1992.
[18] L. M. Stuart *et al.*, Report No. SLAC-PUB-6305 (unpublished).
[19] P. E. Bosted *et al.*, Phys. Rev. C **46**, 2505 (1992).
[20] H. M. Roder *et al.*, NMR report, 1972 (unpublished).
[21] NBS Cryogenic Data Center Memorandum, M4 and M9 (unpublished).
[22] NPAS Users Guide, SLAC Report No. 269, 1984 (unpublished).
[23] L. Mo and C. Peck, SLAC Report No. TN65-29, 1965 (unpublished).
[24] L. Andivahis *et al.*, SLAC Report No. PUB 5753, 1992 (unpublished).
[25] P. Bosted and A. Rahbar, SLAC Report No. NPAS-TN-85-1, 1985 (unpublished).
[26] W. B. Atwood, Ph.D. thesis, Stanford University, 1975.
[27] Y. Tomkiewicz and E. L. Garwin, Nucl. Instrum. Methods **114**, 413 (1973).
[28] Y. S. Tsai, Phys, Rev. **122**, 1898 (1961).
[29] L. W. Mo and Y. S. Tsai, Rev. Mod. Phys. **41**, 205 (1969).
[30] S. D. Drell and S. Fubini, Phys. Rev. **113**, 741 (1959).
[31] G. Höhler *et al.*, Nucl. Phys. **B114**, 505 (1976), fit 5.3.
[32] F. Iachello, A. D. Jackson, and A. Lande, Phys. Lett. **43B**, 191 (1973).
[33] S. J. Brodsky and G. R. Farrar, Phys. Rev. Lett. **31**, 1153 (1973); Phys. Rev. D **11**, 1309 (1975).
[34] S. Furuichi and K. Watanabe, Prog. Theor. Phys. **82**, 581 (1989); **83**, 565 (1990); **84**, 1188 (1990).
[35] M. Gari and W. Krümpelmann, Phys. Lett. **141B**, 295 (1984); Z. Phys. A **322**, 689 (1985).
[36] M. A. Shifman, A. I. Vainshtein, and V. I. Zakharov, Nucl. Phys. **B147**, 385 (1979); **B147**, 448 (1979); **B147**, 519 (1979).
[37] A. V. Radyushkin, Acta Phys. Pol. B **15**, 403 (1984).
[38] P. L. Chung and F. Coester, Phys. Rev. D **44**, 229 (1991), model with $m_q = 0.24$ GeV.
[39] M. Warns, H. Schröder, W. Pfeil, and H. Rollnik, Z. Phys. C **45**, 613 (1990); **45**, 627 (1990).
[40] P. Kroll, M. Schürmann, and W. Schweiger, Z. Phys. A **338**, 339 (1991), model using DA 2.13.
[41] G. P. Lepage and S. J. Brodsky, Phys. Rev. Lett. **43**, 545 (1979).
[42] G. P. Lepage and S. J. Brodsky, Phys. Rev. D **22**, 2157 (1980).
[43] H. Crannell, Nucl. Instrum. Methods **71**, 208 (1974).
[44] P. N. Kirk *et al.*, Phys. Rev. D **8**, 63 (1973).
[45] R. C. D. Walker, Ph.D. thesis, California Institute of Technology, 1989.

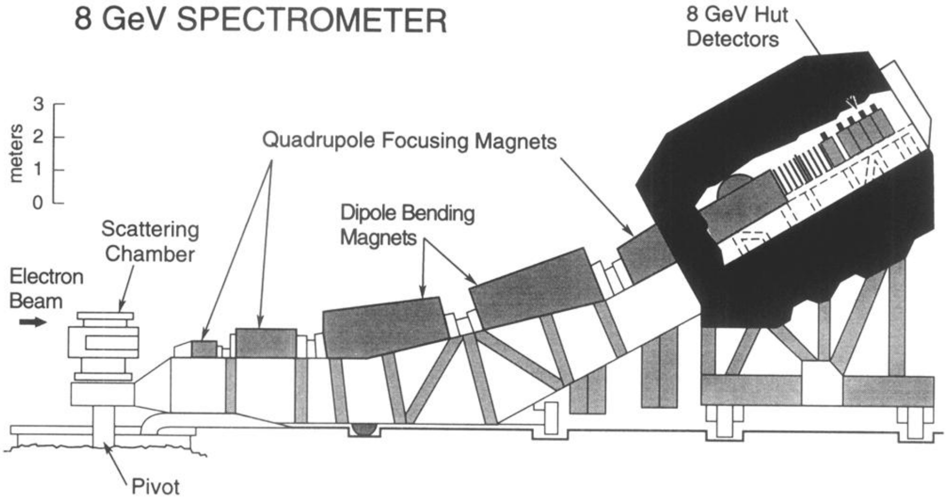

FIG. 6. The 8 GeV spectrometer. Three quadrupoles Q81, Q82, and Q83, provided focusing while two 15° vertical bend dipoles B81 and B82 provided the momentum dispersion. The spectrometer was rotated between 13.2° – 90°, and operated at central momenta between 0.6 – 7.7 GeV/c.

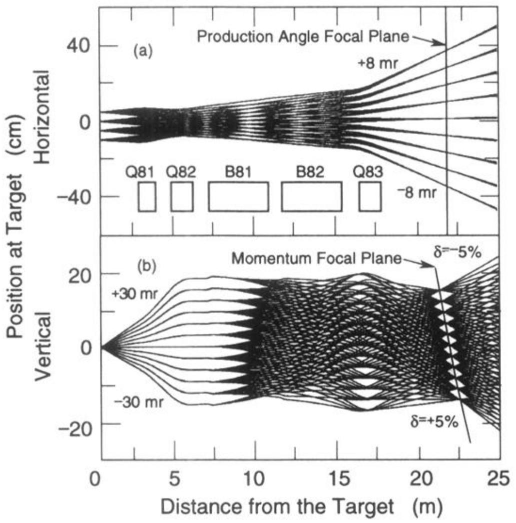

FIG. 7. The horizontal (a) and vertical (b) optics for the 8 GeV spectrometer. The boxes indicate the location of the magnets. The momentum focal plane is tilted at a steep angle of 13.9° relative to the central ray due to chromatic aberrations.

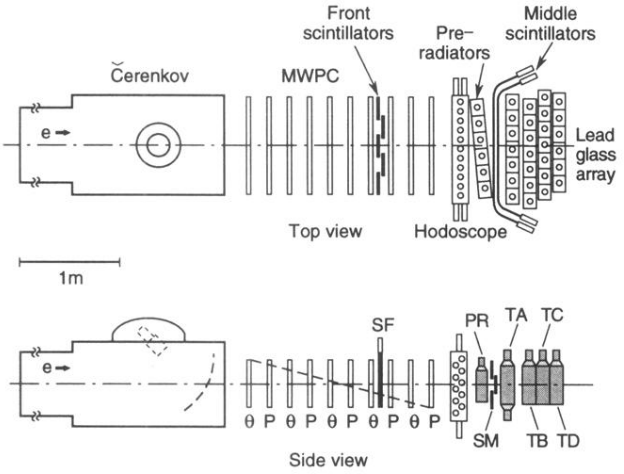

FIG. 8. The 8 GeV detectors. The detector package contained a nitrogen-filled Čerenkov detector followed by ten planes of multiwire proportional chambers and a lead glass shower counter. Two planes of scintillators were interspersed and a hodoscope was installed prior to the lead glass array. The momentum focal plane cuts diagonally through the wire chambers as indicated by the dashed line.

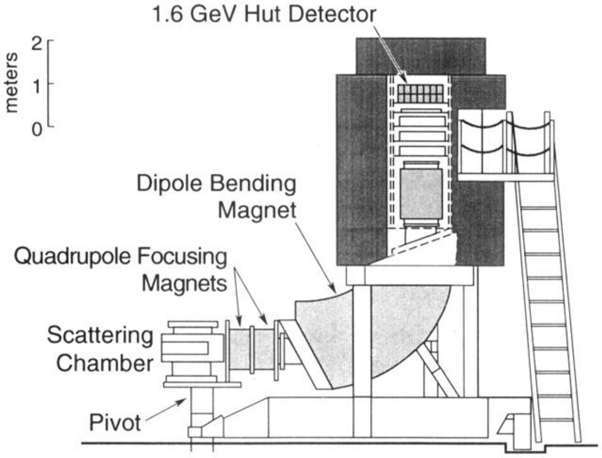

FIG. 9. The 1.6 GeV spectrometer. Two quadrupoles, Q1 and Q2, were placed prior to the 90° vertical bend dipole, B1, to increase the solid angle by a factor of three. The spectrometer remained fixed at 90°, and operated at central momenta between $0.1 - 0.8$ GeV/c.